Gut–liver translocation of pathogen *Klebsiella pneumoniae* promotes hepatocellular carcinoma in mice

Xueliang Wang[1,2,3,8], Yi Fang[3,8], Wei Liang[3,8], Yuhong Cai[1,8], Chi Chun Wong[2], Junlin Wang[3], Na Wang[3], Harry Cheuk-Hay Lau [2], Ying Jiao[2], Xingyu Zhou[2], Liufang Ye[2], Mengmiao Mo[3], Tao Yang[3], Miao Fan[3], Lei Song[3], Heming Zhou [2], Qiang Zhao[4], Eagle Siu-Hong Chu[2], Meinong Liang[3], Weixin Liu [2], Xin Liu [1], Shuaiyin Zhang[3], Haitao Shang[3], Hong Wei[3], Xiaoxing Li[3], Lixia Xu[5], Bing Liao[6], Joseph J. Y. Sung [2,7], Ming Kuang [1] & Jun Yu [2,3] ✉

Hepatocellular carcinoma (HCC) is accompanied by an altered gut microbiota but whether the latter contributes to carcinogenesis is unclear. Here we show that faecal microbiota transplantation (FMT) using stool samples from patients with HCC spontaneously initiate liver inflammation, fibrosis and dysplasia in wild-type mice, and accelerate disease progression in a mouse model of HCC. We find that HCC-FMT results in gut barrier injury and translocation of live bacteria to the liver. Metagenomic analyses and bacterial culture of liver tissues reveal enrichment of the gut pathogen *Klebsiella pneumoniae* in patients with HCC and mice transplanted with the HCC microbiota. Moreover, *K. pneumoniae* monocolonization recapitulates the effect of HCC-FMT in promoting liver inflammation and hepatocarcinogenesis. Mechanistically, *K. pneumoniae* surface protein PBP1B interacts with and activates TLR4 on HCC cells, leading to increased cell proliferation and activation of oncogenic signalling. Targeting gut colonization using *K. oxytoca* or TLR4 inhibition represses *K. pneumoniae*-induced HCC progression. These findings indicate a role for an altered gut microbiota in hepatocarcinogenesis.

Hepatocellular carcinoma (HCC) is a leading cause of cancer-associated deaths[1]. HCC proceeds via a multistep cascade involving liver inflammation, fibrosis, cirrhosis and HCC[2]. Beyond host factors, gut dysbiosis plays important roles in HCC pathogenesis[3]. Recent studies have also unravelled the existence of an intratumoural microbiome[4] that promotes tumorigenesis and modifies the immune microenvironment[5–8]. However, the function of gut and intrahepatic microbes in HCC pathogenesis remains largely unclear.

The gut microbiome regulates liver homoeostasis via the gut–liver axis[9,10]. The gut barrier is the first line of defence against deleterious gut pathogens and their products, and a leaky gut might enable transfer of gut microbes to the liver in disease states[11]. Intriguingly, germ-free mice displayed delayed HCC progression due to reduced activation of Toll-like receptor 4 (TLR4)[12], a sensor of bacterial infection. This highlights the possibility that gut dysbiosis may contribute to hepatocarcinogenesis.

Here we sought to establish the causality of HCC-associated gut dysbiosis in promoting HCC. We performed faecal microbiota transplantation (FMT) of microbial consortia from patients with HCC and healthy donors to mice, revealing that HCC-FMT promotes inflammation, fibrosis, dysplasia and HCC. HCC-associated gut microbiota disrupts gut barrier function and promotes translocation of live

bacteria to the liver, especially *Klebsiella pneumoniae* (*K. pneumoniae*). *K. pneumoniae* monocolonization studies in mice validated its causative role in HCC. Mechanistically, HCC-FMT and *K. pneumoniae* activate hepatic inflammatory and oncogenic signalling. Corroborating these results, live *K. pneumoniae* is enriched in liver tissues of individuals with HCC. Altogether, we revealed a causative role of gut dysbiosis in hepatocarcinogenesis.

Results

HCC stool accelerates DEN-induced liver tumorigenesis

We initially investigated the effect of polymicrobial consortia transplantation from stool of patients with HCC or liver cirrhosis (LC) and healthy donors on liver pathologies in germ-free and specific pathogen-free (SPF) mice. 16S ribosomal (r)RNA sequencing revealed a progressive decrease in microbial diversity in stool samples from healthy donors, LC to HCC, as determined by Shannon, Chao1 and Ace indices (Supplementary Fig. 1a). *Klebsiella* was highly enriched in stool samples from individuals with HCC (Supplementary Fig. 1a). We observed accurate recapitulation of gut microbiome differences of donor consortia in germ-free mice stool after FMT treatment (Supplementary Fig. 1b,c), as evidenced by reduced microbial diversity and enrichment of *Klebsiella* in mice receiving HCC-FMT compared with other groups.

Faecal microbiota consortia were transplanted from 15 HCC (GFD/HCC-FMT), 17 LC (GFD/LC-FMT) and 16 healthy donors (GFD/HD-FMT) to diethylnitrosamine (DEN)-injected germ-free (GFD) mice once per week (Fig. 1a), with PBS as blank control. Compared with the other groups, HCC-FMT increased maximum tumour diameter ($P = 0.007$ vs LC-FMT; $P < 0.0001$ vs HD-FMT), tumour number ($P = 0.0001$ vs HD-FMT) and tumour burden ($P = 0.0012$ vs LC-FMT; $P < 0.0001$ vs HD-FMT) (Fig. 1b and Supplementary Fig. 2a), indicating that HCC-associated microbes promote tumorigenesis. Immunohistochemistry (IHC) showed that HCC-FMT induced hepatocyte proliferation (PCNA, Ki-67) (Fig. 1c and Supplementary Fig. 2b) compared with LC-FMT and HD-FMT. Meanwhile, HCC-FMT and LC-FMT similarly induced liver inflammation, with increased pro-inflammatory T helper 1 (T_H1) and T_H17 cells, together with reduced anti-inflammatory T_H2 compared with HD-FMT (Supplementary Fig. 2c). Fibrosis markers desmin, α-smooth muscle actin (α-SMA) and Sirius red staining were also increased by HCC-FMT and LC-FMT (Supplementary Fig. 2d). Cancer pathway PCR array revealed that HCC-FMT upregulated genes involved in cell proliferation (*G6pdx*, *Skp2*, *Pgf*, and *Sox10*), angiogenesis and embryonic development (*Angpt2* and *Gsc*), epithelial–mesenchymal transition (*Foxc2* and *Snai1*) and anti-apoptosis (*Epo*) compared with LC-FMT and HD-FMT (Fig. 1d). Inflammatory response and autoimmunity PCR array showed that pro-inflammatory response (*Tlr4*, *Tnfsf14*, *Il6ra*, *Ccl4*, and *Tlr2*) and lymphocyte chemotaxis (*Ccr2* and *Cxcr2*) were increased by HCC-FMT compared with LC-FMT and HD-FMT groups (Fig. 1e).

The protumorigenic effect of HCC-FMT compared with LC-FMT and HD-FMT were recapitulated in DEN-injected SPF mice (Fig. 1f–j and Supplementary Fig. 3a–d) and validated by another mixed stool consortium from HCC ($N = 5$) and healthy donors ($N = 5$) in DEN-injected germ-free mice (Extended Data Fig. 1a–d). Furthermore, individual FMT from healthy donors ($N = 2$) and patients with HCC ($N = 2$) to DEN-injected germ-free mice again showed that HCC-FMT accelerated HCC progression (Extended Data Fig. 1e–h). Together, faecal transplantation of HCC microbiota to mice accelerates DEN-induced HCC progression.

HCC stool promotes inflammation, fibrosis and dysplasia

Next, we performed FMT of polymicrobial consortia from 16 patients with HCC (GF/HCC-FMT) and 12 healthy donors (GF/HD-FMT) to germ-free mice without DEN injection (Extended Data Fig. 2a). Upon killing, mice receiving HCC-FMT displayed liver nodules (in 9 out of

16 mice) that were absent from HD-FMT and PBS groups ($P < 0.0001$) (Extended Data Fig. 2b). Haematoxylin and eosin (H&E) staining confirmed diagnosis of dysplasia in the HCC-FMT group (Extended Data Fig. 2b). Compared with HD-FMT, HCC-FMT increased hepatocyte proliferation (PCNA and Ki-67) (Extended Data Fig. 2c), hepatic inflammation (T_H1, T_H17 and T_H2) (Extended Data Fig. 2d) and liver fibrosis markers (desmin, α-SMA and Sirius red) (Extended Data Fig. 2e). Cancer pathway PCR array revealed that HCC-FMT upregulated genes involved in cell proliferation (*Cdc20* and *Dkc1*), angiogenesis (*Angpt2*), epithelial–mesenchymal transition (*Foxc2* and *Snai2*) and anti-apoptosis (*Nol3*) (Extended Data Fig. 2f). Inflammatory response and autoimmunity PCR array also showed that pro-inflammatory response (*Tlr4*, *Myd88*, *Nfkb1* and *Il1a*) and lymphocyte chemotaxis (*Ccl12*, *Ccl11* and *Ccl7*) were increased by HCC-FMT (Extended Data Fig. 2g). Concordant results were obtained by FMT of HCC stool to SPF mice (Extended Data Fig. 3a–f) and of independent stool consortia from individuals with HCC ($N = 5$) and healthy donors ($N = 5$) to germ-free mice (Extended Data Fig. 4a–f). Collectively, HCC-FMT spontaneously induces liver inflammation, fibrosis and dysplasia in mice.

HCC stool promotes gut leakage and pathogen translocation

Gut dysbiosis modulates liver pathologies via the gut–liver axis[13]. We examined the effect of FMT treatment on gut barrier integrity and demonstrated that HCC-FMT increased gut permeability to 500 kDa FITC-dextran (without DEN: $P < 0.0001$; with DEN: $P = 0.0024$) compared with HD-FMT and PBS in germ-free mice (Extended Data Fig. 5a,b). Transmission electron microscopy (TEM) confirmed abnormalities of colon intercellular junctions in HCC-FMT, with disappearance of tight junctions and widening of adherens junctions (Fig. 2a and Supplementary Fig. 4a). HCC-FMT reduced the thickness of colonic mucus and downregulated the expression of tight junction markers (claudin 3 (CLDN3), CLDN1 and E-cadherin (E-cad)), leading to increased bacterial infiltration into mucosal lamina propria and muscularis mucosa (Extended Data Fig. 5a,b, Fig. 2a and Supplementary Fig. 4a). As a result, HCC-FMT induced inflammation in colon, as evidenced by PCR array and flow cytometry (Extended Data Fig. 5c,d). These suggest that HCC-FMT disrupts the gut barrier and promotes bacterial infiltration into colonic mucosa.

We next asked whether disrupted gut barrier function might enable translocation of gut microbes to the liver. Anaerobic and aerobic culture of fresh liver homogenates from germ-free mice demonstrated that almost all liver samples from HCC-FMT displayed positive culture, while those from the HD-FMT group were largely negative ($P < 0.0001$) (Fig. 2b, Extended Data Fig. 5e and Supplementary Fig. 4b). Cultures of the PBS group and contamination controls all tested negative (Fig. 2b, Extended Data Fig. 5f and Supplementary Fig. 4b). Fluorescence in situ hybridization (FISH) (universal 16S rRNA) confirmed that bacteria were readily detected in livers of the HCC-FMT group but were absent in the HD-FMT (close to none) and PBS groups (Extended Data Fig. 5g). TEM of colon and hepatic tissues confirmed the presence of bacteria in HCC-FMT-treated germ-free mice (Fig. 2c). Corroborating these results, gut barrier disruption and translocation of live bacteria to the liver was validated in SPF mice with HCC-FMT (Extended Data Fig. 6a–c), germ-free mice transplanted with another mixed stool consortium from individuals with HCC ($N = 5$) and healthy donors ($N = 5$) (Extended Data Fig. 7a–h), and individual HCC-FMT ($N = 2$) and HD-FMT ($N = 2$) (Extended Data Fig. 7i–k). Notably, LC-FMT evidently caused gut barrier dysfunction and bacterial translocation to the liver, consistent with the involvement of gut dysbiosis in liver pathologies.

To decipher the live bacterial composition in the liver, colonies were randomly selected from liver tissues for identification (Fig. 2d). *K. pneumoniae* was the top bacterium enriched in the HCC-FMT group compared with HD-FMT, followed by *Enterococcus faecalis*, *Proteus mirabilis*, *Enterobacter hormaechei* and *Bacteroides fragilis*
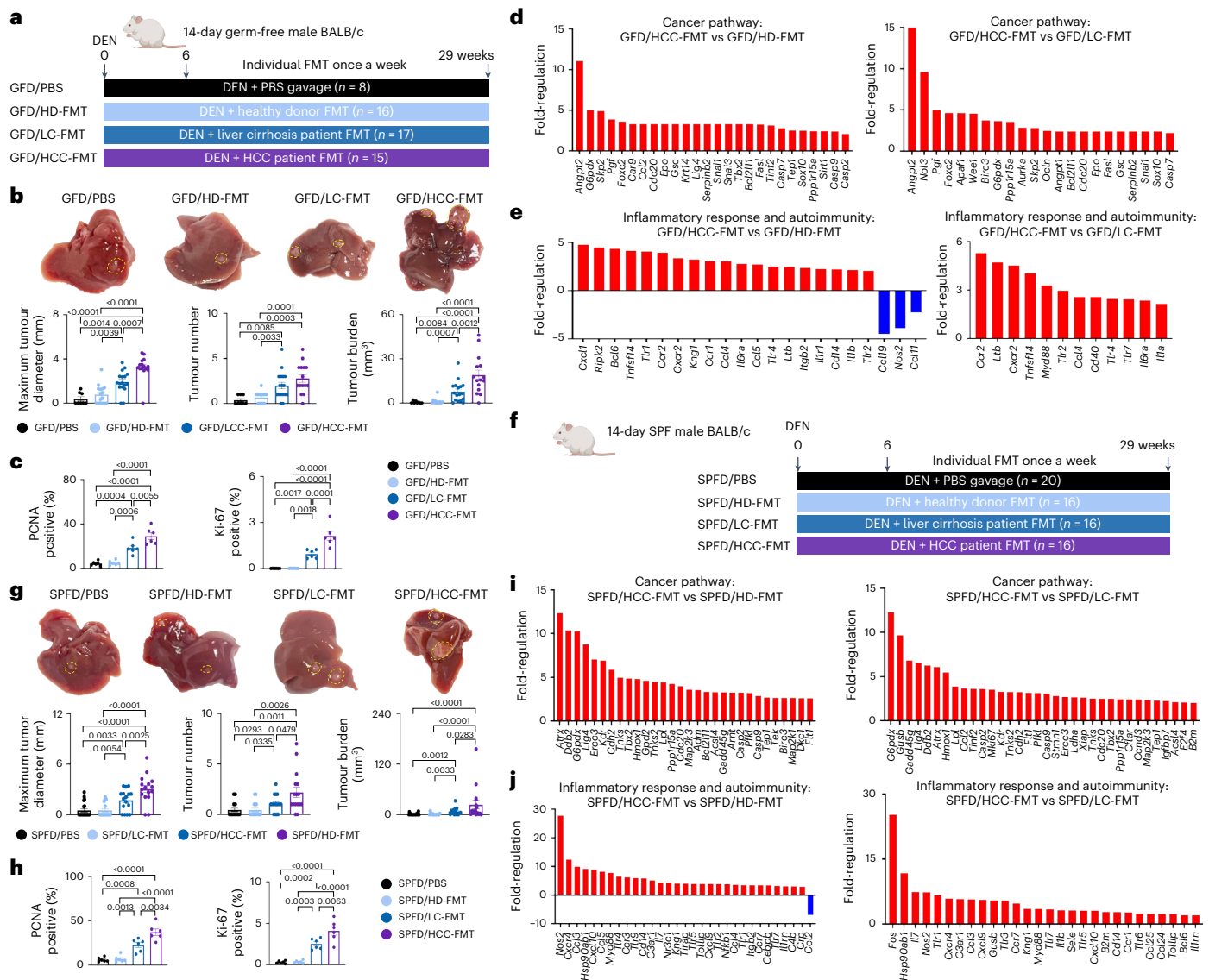
Fig. 1 | Fetal microbiota from patient with HCC promotes HCC in both germ-free and SPF mice with DEN treatment. a, Design of FMT experiment for DEN-treated germ-free mice (GFD/PBS group $n = 8$; GFD/HD-FMT group $n = 16$; GFD/LC-FMT group $n = 17$; GFD/HCC-FMT group $n = 15$) and relevant results (**b–e**). **b**, Representative images of liver gross morphology (dashed yellow circles indicate tumour) with tumour incidence, tumour number and tumour burden. $n = 8$ (GFD/PBS), 16 (GFD/HD-FMT), 17 (GFD/LC-FMT) and 15 (GFD/HCC-FMT) mice. **c**, Immunohistochemistry (IHC) staining for PCNA and Ki-67. $n = 6$ biologically independent samples. **d**, Mouse cancer pathway finder array of liver tissues. **e**, Mouse inflammatory response and autoimmunity PCR array of liver tissues. In **d** and **e**, $n = 3$ independent experiments with similar results. **f**, Design of FMT experiment for DEN-treated SPF mice (SPFD/PBS group $n = 20$;

SPFD/HD-FMT group $n = 16$; SPFD/LC-FMT group $n = 16$; SPFD/HCC-FMT group $n = 16$) and relevant results (**g–j**). **g**, Representative images of liver gross morphology (yellow circles indicate tumour) with tumour incidence, tumour number and tumour burden. $n = 20$ (SPFD/PBS), 16 (SPFD/HD-FMT), 16 (SPFD/LC-FMT), 16 (SPFD/HCC-FMT). **h**, IHC staining for PCNA and Ki-67. $n = 6$ biologically independent samples. **i**, Mouse cancer pathway finder array of liver tissues. $n = 3$ biologically independent samples of each group were mixed for assay. **j**, Mouse inflammatory response and autoimmunity PCR array of liver tissues. In **i** and **j**, $n = 3$ independent experiments with similar results. In **b**,**c**,**g**,**h**, data are presented as mean ± s.e.m. Each data point in bar plots represents one mouse. Statistical significance was calculated using one-way ANOVA. Adjustments were made for multiple comparisons.

(Fig. 2d). Absolute quantification by qPCR in human donors and recipient mouse samples demonstrated that faecal *K. pneumoniae* was increased in individuals with HCC compared with those with LC and healthy donors, and a consistent pattern was reproduced in the stool of FMT recipient mice (Fig. 2e). Correspondingly, liver *K. pneumoniae* levels were higher in the HCC-FMT group compared with LC-FMT and HD-FMT groups (Fig. 2e), which was confirmed by FISH using a *K. pneumoniae*-specific probe (Fig. 2f). Together, HCC-associated gut dysbiosis disrupts gut barrier function, thereby promoting translocation of bacteria to the liver and enrichment of intrahepatic *K. pneumoniae*.

Live *K. pneumoniae* is enriched in liver tissue of patients with HCC

We next sought to validate our discoveries in human patients. Universal 16S rRNA FISH of tissue arrays revealed the enrichment of bacteria in tumorous compared with the paracancerous region in patients with HCC ($P < 0.0001$) ($N = 45$) (Supplementary Fig. 5a). Anaerobic and aerobic culture of fresh liver homogenates from 54 individuals with HCC and 15 with LC demonstrated a living microbiome in HCC and LC tissues, which were confirmed by FISH, lipopolysaccharide (LPS) and lipoteichoic acid (LTA) staining (Fig. 3a,b). Mass spectrometry identification of randomly picked live bacterial colonies and 16S rRNA
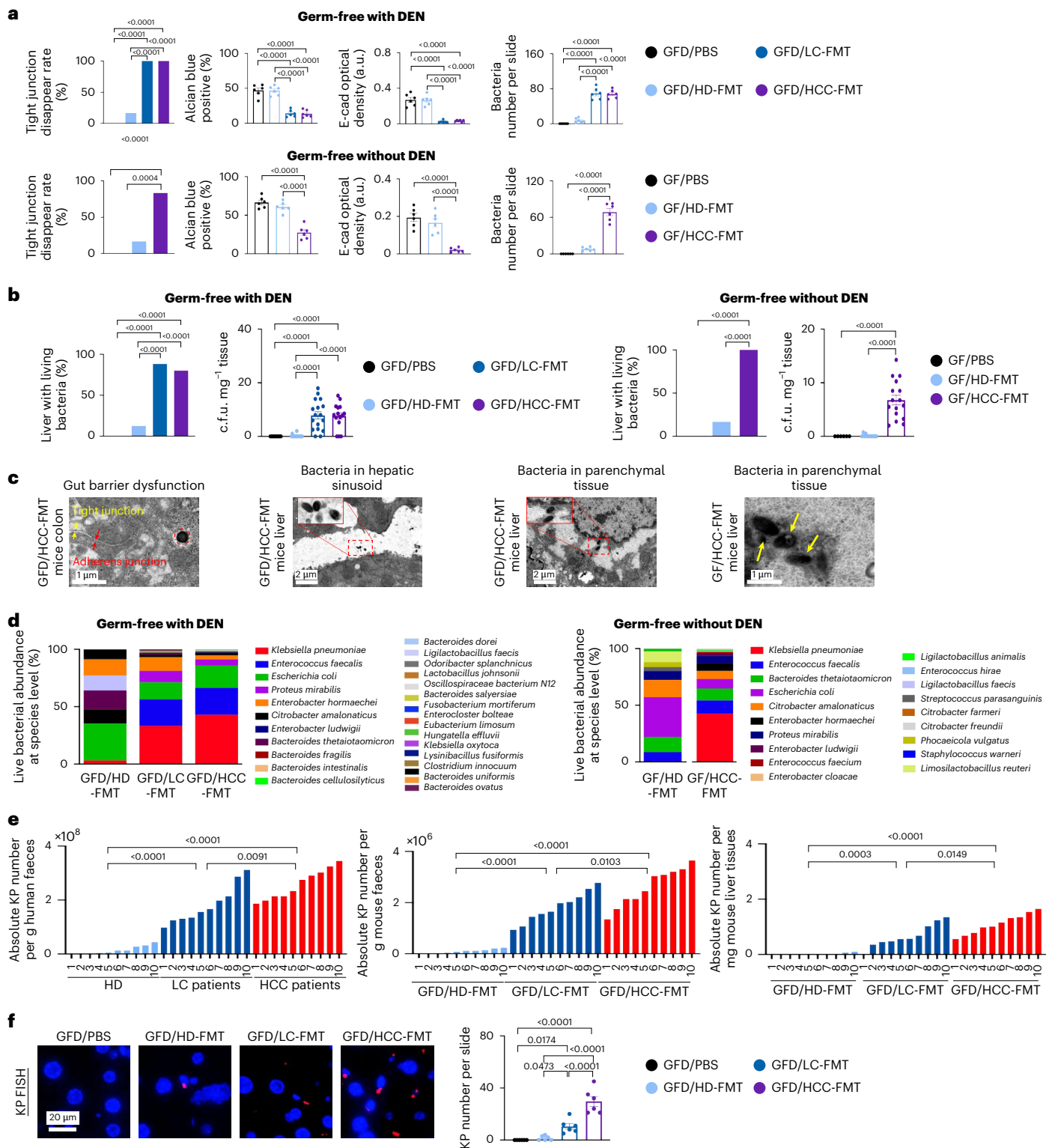
Fig. 2 | Faecal microbiota from patients with HCC impairs gut barrier function and promotes bacteria translocation to the liver in germ-free mice with or without DEN treatment. a, Quantitative analysis of TEM, Alcian blue staining, E-cad IHC staining and Cy3-conjugated EUB338 probe FISH of colon tissues. $n = 6$ biologically independent samples. **b**, Quantitative analysis of bacterial culture of liver tissues under anaerobic and aerobic conditions with quantitative analysis. $n = 8$ (GFD/PBS), 16 (GFD/HD-FMT), 17 (GFD/LC-FMT), 15 (GFD/HCC-FMT), 6 (GF/PBS), 12 (GF/HD-FMT), 16 (GF/HCC-FMT) mice. **c**, Representative TEM images of colon tissues and liver tissues in GFD/HCC-FMT mice and representative TEM image of liver tissues in GF/HCC-FMT mice. $n = 3$ independent experiments with similar results. **d**, Stacked bar plot of relative abundance of culturable

bacterial strains as determined by microbial mass spectrometry identification. **e**, Absolute number of *K. pneumoniae* (KP) in human faeces (left), mice faeces (middle) and mice liver tissues (right) as detected by qPCR. $n = 10$ biologically independent samples. **f**, Representative images (left) and quantification (right) of Cy3-conjugated *K. pneumoniae* probe FISH detection in mice liver tissues. $n = 6$ biologically independent samples. In **a** (excluding tight junction disappear rate), **b** (excluding liver with living bacteria) and **f**, data are presented as mean ± s.e.m. Each data point in bar plots represents one mouse. Tight junction disappearance rate and liver with living bacteria were analysed using Fisher's exact test. Unless otherwise stated, statistical significance was calculated using one-way ANOVA. Adjustments were made for multiple comparisons.

sequencing (Fig. 3c,d) revealed that *Klebsiella* (*K. pneumoniae*) dominates the liver microbiome of individuals with HCC compared with LC, which was supported by absolute quantification (*P* = 0.0002) and *K. pneumoniae*-specific FISH probe (*P* < 0.0001) (Fig. 3e,f). Finally, we demonstrated that upregulation of faecal *K. pneumoniae* in individuals with HCC negatively correlated with overall survival and progression-free survival of HCC patients (Supplementary Fig. 5b). These results implicate a living hepatic microbiome in individuals with HCC with preferential enrichment of *K. pneumoniae*.

K. pneumoniae initiates gut barrier disruption by gelatinase

To identify the driver bacterium in promoting HCC, we next selected 5 top enriched Gram-negative bacteria (*K. pneumoniae*, *Bacteroides thetaiotaomicron* (BT), *Enterobacter hormaechei* (EH), *Escherichia coli* (EC) and *P. mirabilis* (PM)) from liver tissues of HCC-FMT-treated mice and gavaged them to germ-free mice for 10 weeks (Fig. 4a). Compared with PBS control, only *K. pneumoniae* elevated gut permeability (*P* < 0.0001) and translocated to the liver as live bacteria (Fig. 4b). Moreover, *K. pneumoniae* disrupted colonic intercellular junctions, reduced thickness of colonic mucus, downregulated expression of tight junction proteins (E-cad, CLDN3 and CLDN1) and increased bacterial infiltration into mucosal lamina propria and muscularis mucosa (Fig. 4c and Extended Data Fig. 8a), while other candidates had no effect. This suggests that *K. pneumoniae* as a driver bacterium that disrupts the gut barrier to enable its translocation to the liver.

Breakdown of extracellular matrix by gelatinase is the initial step in the invasion of pathogens into gut mucosa[14]. We thus assessed faecal gelatinase activities in germ-free mice treated with individual bacteria. Only faecal supernatants from the *K. pneumoniae* group liquefied gelatin, suggesting gelatinase activity (Supplementary Fig. 6a). Gelatin zymography indicated Collagenase IV activity, as evidenced by clear bands at 72 kDa and 92 kDa (Supplementary Fig. 6b). Matrix metallopeptidase (MMP) activity assays validated the elevated MMP-2/-9 (type IV collagenases) activities in faecal supernatant from mice treated with *K. pneumoniae* (Supplementary Fig. 6c). Consistent with in vitro data, Masson's trichrome staining revealed collagen depletion in colonic mucosa of *K. pneumoniae*-gavaged germ-free mice compared with other bacteria or PBS, which was confirmed by IHC of collagen type IV (COLIV) and fibronectin (Supplementary Fig. 6d). In this connection, faecal supernatants from individuals with HCC and LC exhibited increased gelatinase activity (Supplementary Fig. 7a), as did faecal supernatants from HCC-FMT- and LC-FMT-treated mice (Supplementary Fig. 7b). The direct effect of MMP-2/-9 in attenuating gut barrier markers (COLIV, fibronectin, E-cad and ZO-1) was demonstrated in normal NCM460 cells (Supplementary Fig. 7c). Hence, *K. pneumoniae* and HCC-FMT disrupt colonic barrier function by promoting gelatinase activity.

Interestingly, *K. pneumoniae*-conditioned medium lacks gelatinase activity (Supplementary Fig. 8a–c), implying an indirect effect of this bacterium. Macrophages are known to secrete MMP-2/-9 (refs. 15,16), which could damage gut barrier integrity[17]. We thus

asked whether *K. pneumoniae* might boost macrophage-derived MMP-2/-9. Supporting our notion, in vitro co-culture of THP-1-induced macrophages with *K. pneumoniae*-conditioned medium induced MMP-2/-9 activity, as assessed by gelatin hydrolysis assay and gelatin zymography assays (Fig. 4d). To test this hypothesis in vivo, we depleted macrophages in germ-free mice using Clodrosome, followed by gavage of *K. pneumoniae* (Fig. 4e–h and Extended Data Fig. 8b–d). Before collection, we gavaged these mice with Cy5.5-ᴅ-Lys-labelled *K. pneumoniae* (Supplementary Fig. 9a) to trace its fate in vivo. While the *K. pneumoniae*-only group showed positive fluorescence and culture in liver tissues with 100% incidence, Clodrosome pretreatment reduced intrahepatic *K. pneumoniae* (2 out of 6) (Fig. 4f). *K. pneumoniae*-specific FISH confirmed that *K. pneumoniae* levels were reduced in livers of macrophage-depleted mice (Extended Data Fig. 8c). Macrophage depletion also alleviated *K. pneumoniae*-promoted gut barrier dysfunction, gelatinase activity (Fig. 4g), collagen degradation (Supplementary Fig. 9b), disruption of colonic intercellular junctions and bacterial infiltration into gut mucosa (Fig. 4h, Extended Data Fig. 8d and Supplementary Fig. 9c). Consequently, Clodrosome relieved *K. pneumoniae*-induced liver pathologies (Supplementary Fig. 9d,e) and oncogenic and pro-inflammatory signalling (Supplementary Fig. 9f,g). Overall, *K. pneumoniae* initiates gut barrier disruption by elevating macrophage-mediated gelatinase activity, which facilitates its eventual translocation to the liver.

K. pneumoniae promotes precancerous lesions and HCC in mice

To validate the function of *K. pneumoniae* in HCC, we gavaged *K. pneumoniae* to germ-free mice (GF/KP) for 36 weeks (Fig. 5a), with *E. coli* MG1655 (GF/EC) and PBS as controls. Fluorescence tracing of Cy5.5-ᴅ-Lys-labelled *K. pneumoniae* and *E. coli* identified *K. pneumoniae*-derived signals in both the gut and liver, whereas *E. coli* signals were restricted to the gut (Supplementary Fig. 10a and Fig. 5b). Bacterial culture and FISH showed the presence of live *K. pneumoniae* in GF/KP mouse liver (8 out of 10), whereas *E. coli* and PBS were both negative (Fig. 5b). These results indicate that monocolonization with *K. pneumoniae* is sufficient for its translocation to the liver. We confirmed previous observations that *K. pneumoniae* compromised gut barrier function by inducing gelatinase activity (Fig. 5c–e, Extended Data Fig. 8e and Supplementary Fig. 10b,c). Critically, *K. pneumoniae*-gavaged germ-free mice developed dysplasia that were absent in *E. coli* or PBS-gavaged mice (*P* < 0.0001) (Fig. 5f). *K. pneumoniae* also induced hepatocyte proliferation (Fig. 5g and Extended Data Fig. 8f), fibrotic injury (Fig. 5h and Extended Data Fig. 8g) and oncogenic and pro-inflammatory signalling (Extended Data Fig. 8h). In addition, the protumorigenic effect of *K. pneumoniae* was further reproduced in SPF mice (Fig. 5i–n and Supplementary Fig. 11a–d) and DEN-injected SPF mice (Fig. 5o,p and Supplementary Fig. 12a–g). In these models, *K. pneumoniae* disrupted gut barrier integrity and translocated to the liver. Our results implicate *K. pneumoniae* as a gut pathogen that promotes precancerous lesions and HCC in mice.


Fig. 3 | Live bacteria, especially *K. pneumoniae*, are enriched in tumour tissues of patients with HCC. a, Top: representative images of bacterial culture of liver tissues from patient with LC under anaerobic and aerobic conditions. *N* = 15 biologically independent samples. From left to right and top to bottom, the culture plates are blood agar plates, chocolate blood agar plates, MacConkey agar plates and Columbia blood agar plates, respectively. Bottom: Cy3-conjugated EUB338 probe FISH detection, LPS and LTA IHC staining of liver tissues from patient with LC (*n* = 3 independent experiments with similar results). **b**, Top: representative images of bacterial culture of tumour tissues from patient with HCC under anaerobic and aerobic conditions. *N* = 54 biologically independent samples. From left to right and top to bottom, the culture plates are blood agar plates, chocolate blood agar plates, MacConkey agar plates and Columbia blood agar plates, respectively. Bottom: Cy3-conjugated EUB338

probe FISH detection, LPS and LTA IHC staining of HCC patient liver tissues (*n* = 3 independent experiments with similar results). **c**, Stacked bar plot of relative abundance of culturable bacterial strains from liver tissues from individuals with LC or with HCC as determined by microbial mass spectrometry identification. **d**, Stacked bar plot of relative abundance at genus level of bacteria from liver tissues from patients with LC or HCC as detected by 16S rRNA sequencing. *N* = 11 (LC), 35 (HCC). **e**, Absolute number of *K. pneumoniae* in liver tissues from patient with LC and HCC as detected by qPCR. *n* = 10 biologically independent samples. **f**, Representative images of Cy3-conjugated *K. pneumoniae* probe FISH detection in liver tissues from patient with LC (top) and HCC (bottom). *n* = 10 biologically independent samples. In **f**, data are presented as mean ± s.e.m. Each data point in bar plots represents one participant. Statistical significance was calculated using Student's *t*-test.

K. pneumoniae cell wall protein binds to and activates TLR4

We next investigated the molecular mechanism of *K. pneumoniae* in HCC. Because *K. pneumoniae*-conditioned medium (KPCM) had no effect on HCC cell viability (Supplementary Fig. 13a,b), we hypothesized that bacteria–HCC cells interaction is necessary. In line with this, scanning electron microscopy (SEM), TEM and cell attachment

assay demonstrated attachment of *K. pneumoniae* to Hep3B and Huh7 cells (Fig. 6a). Co-culture of pasteurized *K. pneumoniae* promoted growth of HCC cells and HCC patient-derived organoids by inducing proliferation (Fig. 6b,c), suggesting that surface proteins of *K. pneumoniae* might be involved. To unravel *K. pneumoniae* proteins that interact with HCC receptors, we performed biotin pulldown and
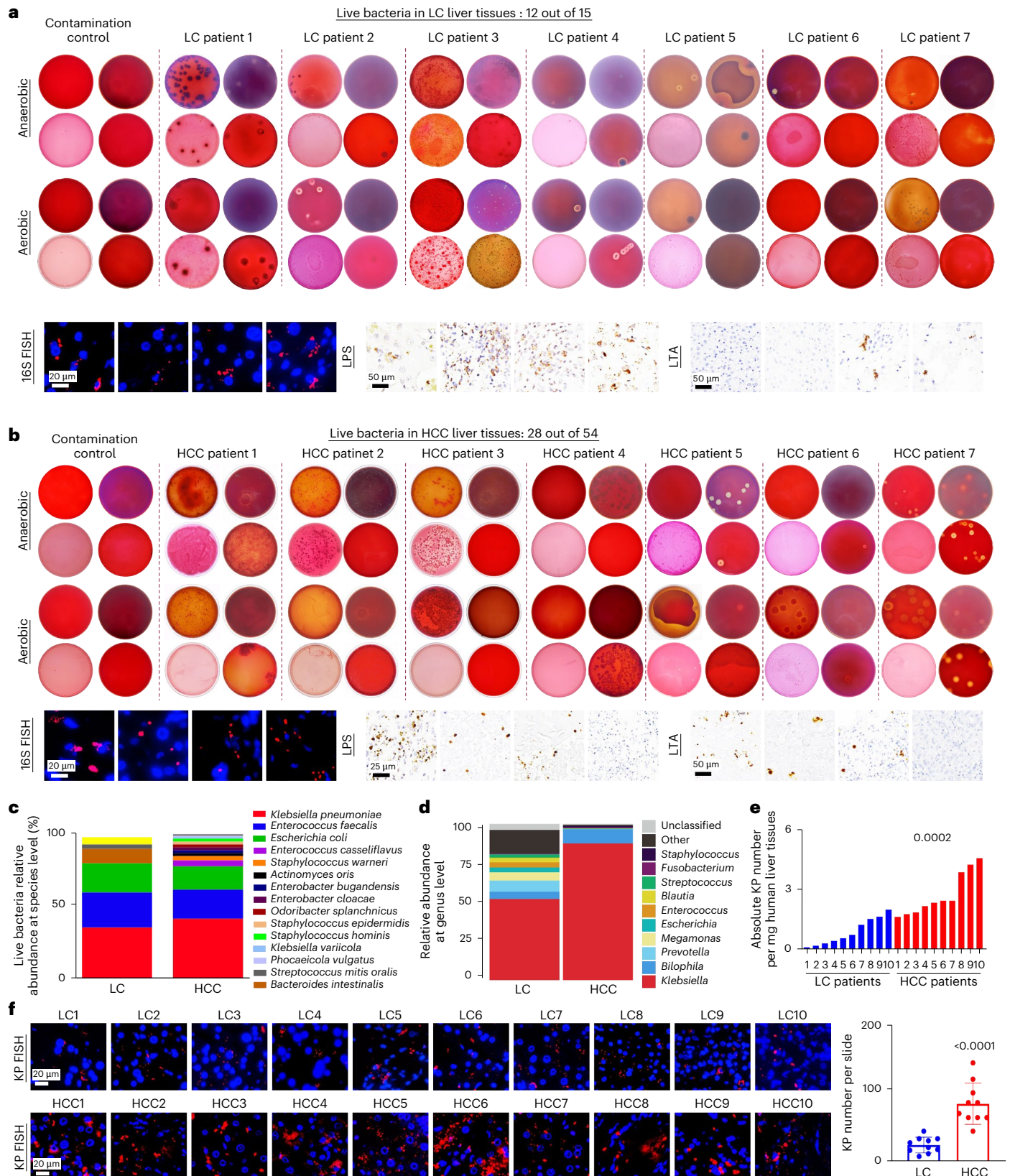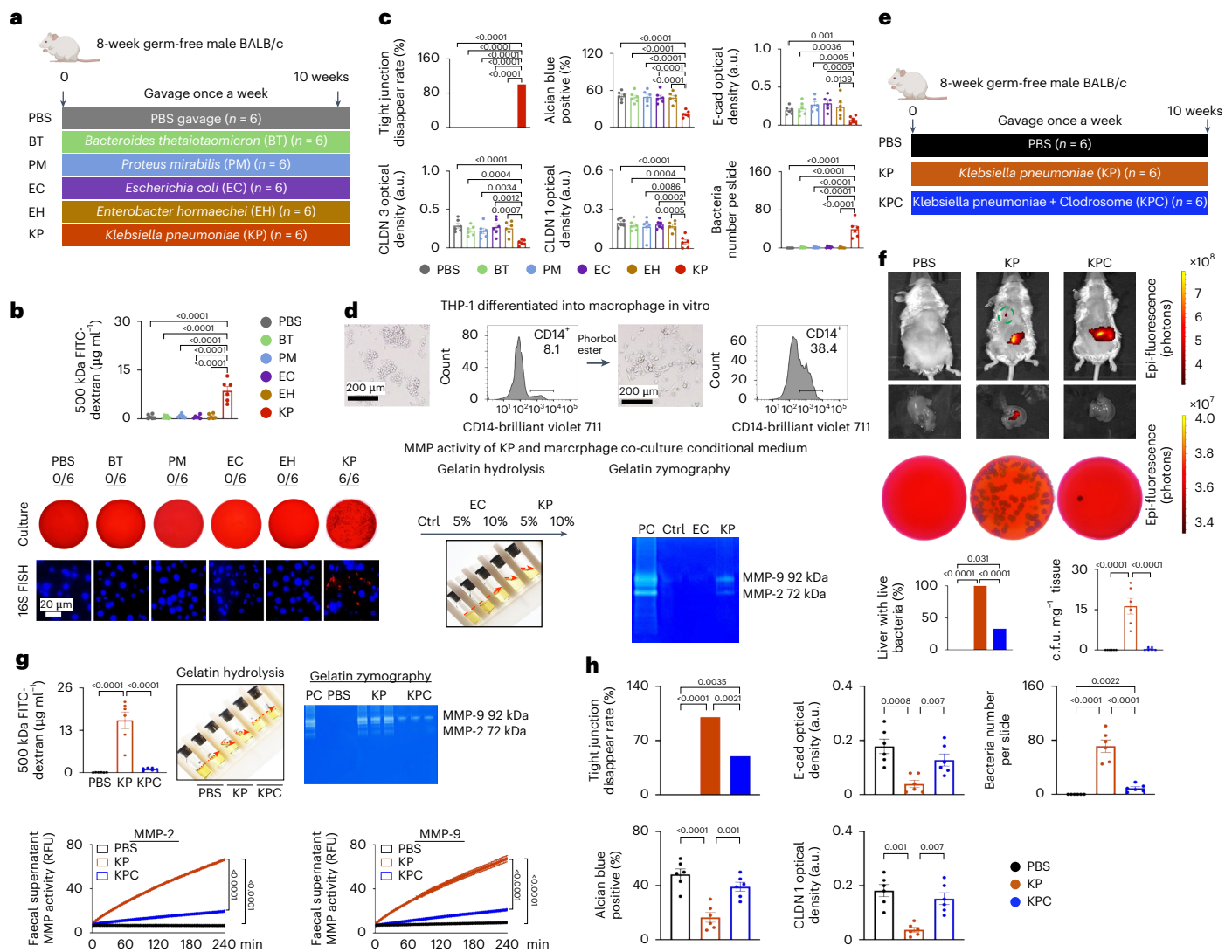
Fig. 4 | *K. pneumoniae* initiates gut barrier dysfunction by elevating colon macrophage-mediated MMP-2/-9 activities. a, Design of 5 Gram-negative bacteria gavage in germ-free mice without DEN (PBS group *n* = 6; BT group *n* = 6; PM group *n* = 6; EC group *n* = 6; EH group *n* = 6; KP group *n* = 6) and related results (**b**,**c**). **b**, Gut permeability assays using 500 kDa FITC-dextran (top), live bacteria translocated into liver cultured in blood agar plates (middle) and Cy3-conjugated EUB338 probe FISH assay of liver tissues (bottom). *n* = 6 biologically independent samples. **c**, Quantitative analysis of TEM, Alcian blue staining, E-cad, CLDN3, CLDN1 IHC staining, and Cy3-conjugated EUB338 probe FISH of colon tissues. *n* = 10 biologically independent samples. **d**, THP-1-induced macrophage using phorbol ester (top row) and MMP-2/-9 activity in *K. pneumoniae* and THP-induced macrophage co-culture conditional medium using gelatin hydrolysis assay and gelatin zymography (bottom row). *n* = 3 independent experiments with similar results. Ctrl: BHI and macrophage co-culture conditional medium; EC: *E. coli* and macrophage co-culture conditional medium; KP: *K. pneumoniae* and macrophage co-culture conditional medium. **e**, Design of colon macrophage depletion using Clodrosome and its effect on *K. pneumoniae*-mediated gut barrier dysfunction in germ-free mice without DEN treatment (PBS group *n* = 6; KP group *n* = 6; KPC group *n* = 6) and related results (**f**–**h**). **f**, In vivo imaging of body and liver after Cy5.5-D-Lys-labelled *K. pneumoniae* gavage (top), and live bacterial culture of liver tissues on blood agar plates and quantification (bottom). *n* = 6 biologically independent samples. **g**, Gut permeability assays using 500 kDa FITC-dextran (top left) (*n* = 6 biologically independent samples) and MMP-2/-9 activity in mouse faecal supernatant detected using gelatin hydrolysis assay (top middle), gelatin zymography (top right) (*n* = 3 independent experiments with similar results) and dynamic activity assay (bottom) (*n* = 6 biologically independent samples). **h**, Quantitative analysis of TEM, Alcian blue staining, E-cad and CLDN1 IHC staining, bacteria number per slide using Cy3-conjugated EUB338 probe (PBS group) and *K. pneumoniae* probe (KP and KPC groups) FISH of colon tissues. *n* = 10 biologically independent samples. In **b**,**c** (excluding tight junction disappear rate) and **f**–**h** (excluding liver with live bacteria and tight junction disappear rate) data are presented as mean ± s.e.m. Each data point in bar plots represents one mouse. Liver with living bacteria and tight junction disappearance rate were analysed using Fisher's exact test. MMP activity was analysed using two-way ANOVA. Unless otherwise stated, statistical significance was calculated using one-way ANOVA. Adjustments were made for multiple comparisons.

identified putative candidates by mass spectrometry (Fig. 6d). One candidate protein, penicillin-binding protein 1B (PBP1B), is reported to localize to the peptidoglycan-based cell wall of *K. pneumonia*. We next constructed glutathione *S*-transferase (GST)-tagged PBP1B (Supplementary Fig. 13c), followed by GST pulldown to identify its corresponding HCC receptor (Fig. 6e and Supplementary Fig. 13d). Overlap of common candidate proteins unravelled TLR4 as a receptor for PBP1B (Fig. 6e and Supplementary Fig. 13d). Surface plasmon resonance (SPR) using purified proteins confirmed direct PBP1B–TLR4 interaction with an affinity of 0.269 nM (Fig. 6f and Supplementary Fig. 13e). In silico modelling showed that PBP1B docks into the TLR4 catalytic site with binding energy of −318 kcal mol^{-1} (Fig. 6g). Co-immunoprecipitation (Co-IP) assays confirmed the interplay between GST–PBP1B and TLR4 in Hep3B and Huh7 cells (Fig. 6h,i).

To investigate whether PBP1B promotes malignant behaviour of HCC cells, we incubated recombinant PBP1B with HCC cells in vitro. PBP1B promoted growth of HCC cells and HCC patient-derived organoids (Fig. 6j). PBP1B robustly increased TLR4, MyD88, p-P65 and PCNA protein levels (Fig. 6k), suggesting TLR4 signalling activation. TLR4 inhibitor (TLR4i; TLR4-IN-C34) abolished PBP1B-induced HCC cell growth (Fig. 6l,m), suggesting TLR4 as its functional target. Furthermore, *K. pneumoniae* gavage to germ-free and SPF mice elevated TLR4 expression (Fig. 6n). Our data suggest that *K. pneumoniae* PBP1B binds to TLR4 in HCC cells, leading to TLR4-mediated tumorigenesis.

Anticolonization or TLR4i reverses *K. pneumoniae*-induced HCC

Given that colonic infiltration of *K. pneumoniae* is obligatory for translocation to the liver, suppressing its colonization in the gut represents a potential therapeutic strategy. *Klebsiella oxytoca* has been reported to promote colonization resistance against pathogens[18,19]. We thus gavaged DEN-treated germ-free mice with *K. oxytoca*, *K. pneumoniae* and *K. oxytoca* plus *K. pneumoniae* (Extended Data Fig. 9a). Remarkably, *K. oxytoca* co-treatment reduced tumour incidence ($P = 0.0027$), tumour number ($P < 0.0001$) and tumour burden ($P = 0.0001$) compared with *K. pneumoniae* alone (Extended Data Fig. 9b). *K. oxytoca* co-treatment also restored gut barrier integrity (Extended Data Fig. 9c,d), thereby preventing infiltration of *K. pneumoniae* into mucosal lamina propria and muscularis mucosa (Extended Data Fig. 9c) and translocation to the liver (Extended Data Fig. 9e and Supplementary Fig. 14a). *K. oxytoca* also abrogated the effect of *K. pneumoniae* on TLR4 activation, hepatocyte proliferation (PCNA, Ki-67) and oncogenic and pro-inflammatory signalling (Supplementary Fig. 14a,b). *K. oxytoca* itself had no effect on HCC development. These results indicate that *K. oxytoca* antagonizes *K. pneumoniae*-induced HCC by arresting its colonic intrusion and translocation to the liver.

Next, we asked whether TLR4 blockade might overcome HCC-promoting *K. pneumoniae* via the PBP1B–TLR4 axis. Supporting our hypothesis, the TLR4i TLR4-IN-C34 reversed the effect of *K. pneumoniae* on tumour incidence ($P = 0.0011$), tumour number ($P < 0.0001$) and tumour burden ($P = 0.0004$) in DEN-injected germ-free mice (Extended Data Fig. 9f,g). Although TLR4-IN-C34 failed to restore the gut barrier or prevent translocation of *K. pneumoniae* to the liver (Extended Data Fig. 9h–j and Supplementary Fig. 15a), it effectively

inhibited TLR4 activation, hepatocyte proliferation (PCNA, Ki-67), fibrosis marker expression, and oncogenic and pro-inflammatory signalling (Extended Data Fig. 9k and Supplementary Fig. 15b–d). TLR4-IN-C34 thus acts by blocking local effects of *K. pneumoniae* in the liver, without impacting gut barrier dysfunction or its translocation to the liver. We also confirmed that TLR4-IN-C34 blocked the HCC-promoting function of HCC-FMT in DEN-treated germ-free mice (Extended Data Fig. 10a,b), an effect independent of gut barrier dysfunction (Extended Data Fig. 10c,d) but is driven by TLR4 downregulation (Extended Data Fig. 10e–g). Collectively, both impairment of gut permeability and local activation of the PBP1B–TLR4 axis in the liver are essential for the HCC-promoting effect of *K. pneumoniae*, which can be targeted to overcome *K. pneumoniae*-induced hepatocarcinogenesis.

Discussion

Here we provide evidence of the causality of HCC-associated gut dysbiosis in contributing to hepatocarcinogenesis. Reconstitution of HCC microbiota in both germ-free mice and SPF mice led to spontaneous liver inflammation, fibrosis and dysplasia, and exacerbated carcinogen-induced HCC. Intriguingly, HCC microbiota was found to impair gut barrier integrity, thereby enabling the transfer of live pathogenic bacteria to the liver and consequential activation of pro-inflammatory and oncogenic signalling to perpetuate tumorigenesis. Characterization of the liver microbiota identified enrichment of pathogenic *K. pneumoniae* in mice given HCC-FMT and in human patients with HCC. Finally, *K. pneumoniae* monocolonization in mice phenocopied the effect of HCC-FMT, corroborating *K. pneumoniae* as an oncogenic pathogen in HCC.

Emerging evidence suggests that gut dysbiosis impacts liver diseases via the gut–liver axis[13]. We investigated this proposition in HCC by transplantation of HCC patient stool to germ-free mice or SPF mice, revealing spontaneous development of liver inflammation and fibrosis, characterized by induction of pro-inflammatory T_H1/T_H17 cells and suppression of anti-inflammatory T_H2 cells. Chronic inflammation and fibrosis are contributors to hepatocarcinogenesis[20]. Indeed, half of HCC-FMT mice developed dysplasia. Furthermore, HCC-FMT accelerated DEN-induced HCC, thus establishing a causative role of HCC-associated dysbiosis in hepatocarcinogenesis.

Gut barrier integrity is fundamental to a functional gut–liver axis, as it prevents indiscriminate access of bacteria and their products

Fig. 5 | *K. pneumoniae* promotes precancerous lesions and HCC in both germ-free and SPF mice. a, Design of *K. pneumoniae* gavage for promoting precancerous lesions in germ-free mice without DEN treatment (GF/PBS group $n = 10$; GF/EC group $n = 8$; GF/KP group $n = 10$) and related results (**b–h**). **b**, In vivo imaging of body and liver after Cy5.5-ᴅ-Lys-labelled *K. pneumoniae* gavage (left), live bacteria culture of liver tissues on blood agar plate (top right) and Cy3-conjugated EUB338 probe (GF/PBS group), *E. coli* probe (GF/EC group) or *K. pneumoniae* probe (GF/KP group) FISH detection in liver tissues (bottom right). **c**, Gut permeability assays using 500 kDa FITC-dextran (left) ($n = 10$ (GF/PBS), 8 (GF/EC), 10 (GF/KP)) and quantitative analysis of TEM (middle) ($n = 6$ biologically independent samples) and E-cad IHC staining (right) ($n = 6$ biologically independent samples). **d**, MMP-2/-9 activity in mouse faecal supernatant using gelatin hydrolysis assay (bottom left), gelatin zymography (top left) and dynamic activity assay (right). $n = 3$ biologically independent samples. **e**, Masson's trichrome staining (top left) and COLIV IHC staining (top right) of colon tissues and COLIV protein level by western blot (bottom). $n = 6$ biologically independent samples. **f**, Representative images of liver gross morphology (top left) (dashed yellow circles indicate nodules), H&E staining of mice liver sections (bottom left), and nodule number and incidence of dysplasia (right). $n = 10$ (GF/PBS), 8 (GF/EC), 10 (GF/KP). **g**, IHC staining for PCNA and Ki-67 (left) ($n = 6$ biologically independent samples), and western blot assay of PCNA (right) ($n = 3$ biologically independent samples). **h**, Desmin (left) and α-SMA (middle) IHC staining, and Sirius red staining (right) of liver sections. $n = 6$ biologically independent samples. **i**, Design of *K. pneumoniae* gavage on precancerous lesions in SPF mice without DEN treatment (PBS group $n = 6$;

EC group $n = 6$; KP group $n = 6$) and relevant results (**j–n**). **j**, Gut permeability assays using 500 kDa FITC-dextran. $n = 6$ biologically independent samples. **k**, Live bacterial culture of liver tissues on blood agar plate (top), and Cy3-conjugated EUB338 probe (PBS group), *E. coli* probe (EC group) or *K. pneumoniae* probe (KP group) FISH detection in liver tissues (bottom). $n = 6$ biologically independent samples. **l**, TEM (left) and quantitative analysis (right) of colon tissues. $n = 6$ biologically independent samples. **m**, Representative images of liver gross morphology (top) (dashed yellow circles indicate nodules), H&E staining of mice liver sections (middle), and nodule number and incidence of dysplasia (bottom). $n = 6$ biologically independent samples. **n**, Representative images of IHC staining for PCNA and Sirius red staining of liver sections (left) with quantitative analysis (right). $n = 6$ biologically independent samples. **o**, Design of *K. pneumoniae* gavage on HCC in SPF mice with DEN treatment (DPBS group $n = 7$; DEC group $n = 6$; DKP group $n = 7$) and related results (**p**). **p**, Representative images of liver gross morphology (left) (dashed yellow circles indicate tumour) and H&E staining of mice liver sections (middle) with tumour incidence and tumour number quantitative analysis (right). $n = 7$ (DPBS), 6 (DEC), 7 (DKP). In **c** (excluding tight junction disappear rate), **d**, **e–h** (excluding incidence of dysplasia), **j,k,m** (excluding incidence of dysplasia), **n** and **p** (excluding tumour incidence), data are presented as mean ± s.e.m. Each data point in bar plots represents one mouse. Tight junction disappearance rate, incidence of dysplasia and tumour incidence were analysed using Fisher's exact test. MMP activity was analysed using two-way ANOVA. Unless otherwise stated, statistical significance was calculated using one-way ANOVA. Adjustments were made for multiple comparisons.

to portal circulation[21]. Here we observed that HCC-FMT increased colonic gelatinase activities. Excess gelatinase activities can degrade extracellular matrix and impair epithelial integrity in the gut[14,22–24]. Gelatinase activity thus has a crucial role in induction of mucosal damage, loss of barrier function and disruption of intestinal tight junctions in HCC-FMT-treated mice. This is manifested by a marked increase in gut permeability after HCC-FMT, exposing the liver to gut pathogens, pathogen-associated molecular patterns and metabolites[25].

Consequently, impaired gut barrier function led to colonization of the liver by live and culturable gut microbes in HCC-FMT-treated mice that were absent in mice given HD-FMT. Although recent studies have described intratumoural microbiota in many cancers[4], the origin of these microbes remains enigmatic. Our results implicate the gut as the origin of intrahepatic pathogens in HCC. Cross-validation in patients with HCC and HCC-FMT-treated mice demonstrated increased *K. pneumoniae* in both stool and liver microbiomes. This is consistent

with a previous study indicating that *Klebsiella* was increased in patients with early HCC[26]. *K. pneumoniae* has been reported to disrupt the intestinal barrier[27–29]; however, its molecular mechanism remains unclear. Here we showed that *K. pneumoniae* promoted macrophage-derived gelatinase activity in colon to induce gut barrier dysfunction. Together, *K. pneumoniae* is a driver pathogen that impairs gut barrier function and enables its own colonization in the liver.

K. pneumoniae is part of the human gut flora (~5% prevalence)[30] and an opportunistic pathogen involved in hepatobiliary infections[31], pyogenic liver abscess[32] and non-alcoholic fatty liver disease[28]; however, its role in tumorigenesis is unknown. We revealed that *K. pneumoniae* exerts protumorigenic function by stimulating the growth of HCC cells and HCC patient-derived organoids. In mice, intrahepatic colonization of *K. pneumoniae* robustly promotes inflammation, fibrosis and oncogenic/inflammation signalling. This indicates *K. pneumoniae* as a gut pathogen promoting hepatocarcinogenesis. In line with our data,
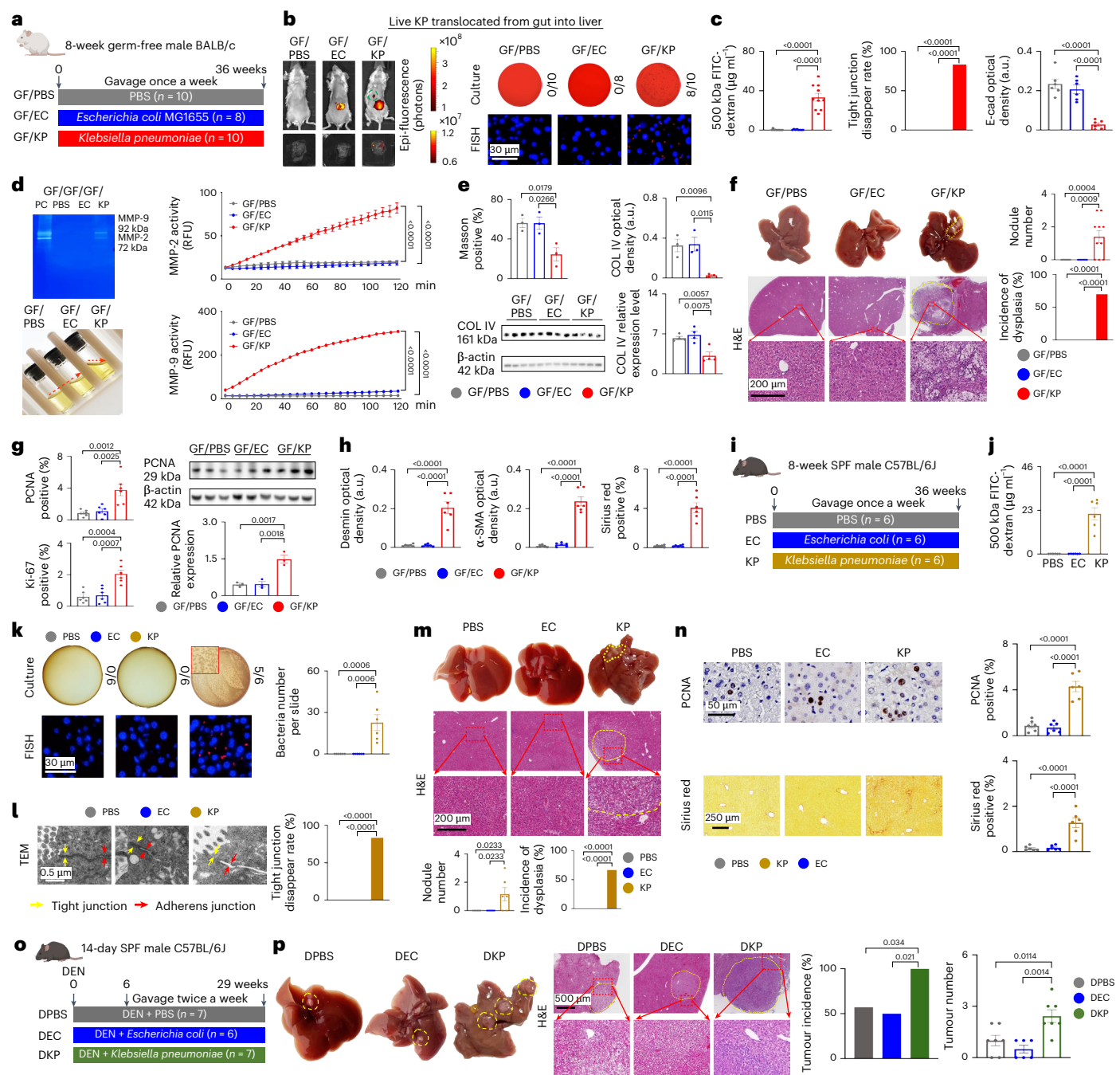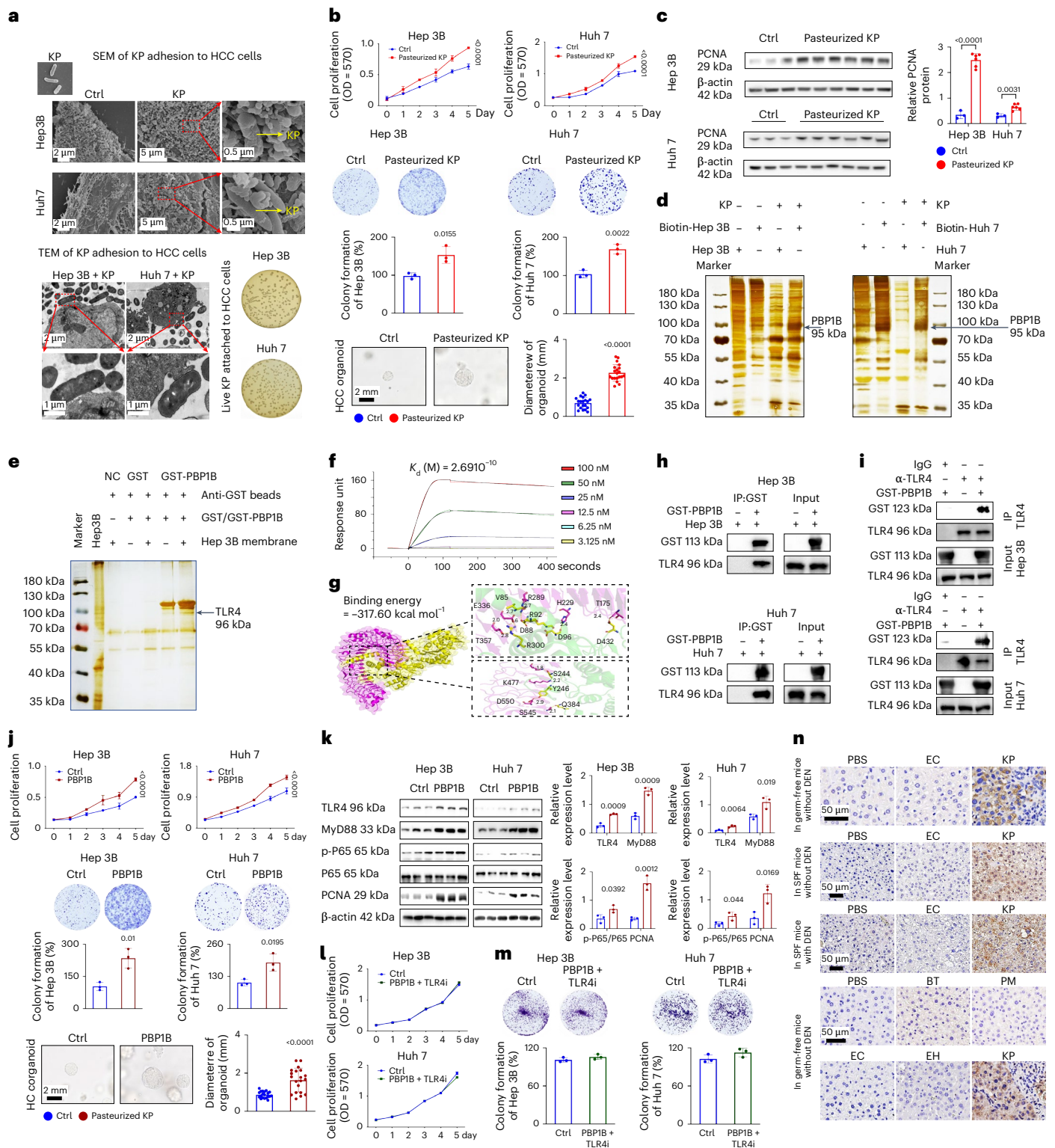
tumour-resident microbiota have been shown to have contributing roles in promoting cancer progression and immunosuppression[7,33].

Mechanistically, *K. pneumoniae* promotes HCC via its surface protein PBP1B, which interacts with and activates TLR4 signalling in HCC cells. Indeed, TLR4 blockade reversed the protumorigenic effect of *K. pneumoniae* and HCC-FMT in mice. Importantly, the abilities of *K. pneumoniae* to disrupt gut barrier integrity and locally activate TLR4 in the liver are both essential for the HCC-promoting effect of this bacterium. Hence, targeting its gut colonization or TLR4

represent viable strategies to repress *K. pneumoniae*-induced HCC progression. Alternatively, recent work showed that *K. pneumoniae* could also be targeted by bacteriophages[34].

In summary, in this study we established a causal link between HCC-associated gut dysbiosis and hepatocarcinogenesis. HCC dysbiosis disrupts gut barrier function and promotes translocation of live, pathogenic bacteria via the gut–liver axis. We identified *K. pneumoniae* as a gut pathogen that initiates gut barrier dysfunction and translocates to the liver, where it exacerbates HCC development via the PBP1B–TLR4

Fig. 6 | *K. pneumoniae* promotes HCC via its surface protein PBP1B binding to and activating TLR4 in HCC cells. a, Representative SEM (top) and TEM (bottom) images of Hep3B and Huh7 HCC cell lines after co-culture with *K. pneumoniae* (MOI = 10). After co-culture of HCC cells with *K. pneumoniae*, cell lysate was spread on BHI agar for bacterial culture. *n* = 3 independent experiments with similar results. **b**, Effect of pasteurized *K. pneumoniae* (MOI = 10) on HCC cell proliferation (top) (*n* = 3 biologically independent samples), colony formation (middle) (*n* = 3 biologically independent samples) and growth of HCC patient-derived organoid (bottom) (*n* = 20 biologically independent samples). **c**, Effect of pasteurized *K. pneumoniae* (MOI = 10) on PCNA expression in HCC cells. *n* = 3 (Ctrl), 6 (pasteurized KP). **d**, Screening of *K. pneumoniae* adhesins by biotin pull-down assay. **e**, Hep3B membrane protein was incubated with GST or GST–PBP1B together with GST magnetic beads for GST pull-down assay. Corresponding bands in GST–PBP1B and Hep3B cell membrane protein groups were subjected to mass spectrometry analysis. In **d** and **e**, *n* = 3 independent experiments with similar results. **f**, Binding affinity between PBP1B and TLR4 was detected using SPR. K_d, dissociation constant. **g**, Representative structure of PBP1B and TLR4 after molecular docking (left) and the residues involved in the interaction between PBP1B with TLR4 (right). The structure of TLR4 is coloured pink while the PBP1B is coloured yellow. The light green dash represents hydrogen bond.

h, TLR4 from Hep3B and Huh7 cell lysates was pulled down by GST–PBP1B according to the GST pull-down assay. **i**, Immunoprecipitation of TLR4 from Hep3B or Huh7 cells lysates validated the binding between TLR4 and GST–PBP1B. In **h** and **i**, *n* = 3 independent experiments with similar results. **j**, Effect of PBP1B (0.05 μM) on HCC cell proliferation (top) (*n* = 3 biologically independent samples), colony formation (middle) (*n* = 3 biologically independent samples) and growth of HCC patient-derived organoid (bottom) (*n* = 20 biologically independent samples). *n* = 3 independent experiments with similar results. **k**, Effect of PBP1B (0.05 μM) on TLR4, MyD88, p-P65, P65 and PCNA protein expression in HCC cells, as determined by western blot. *n* = 3 biologically independent samples. **l,m**, TLR4i (30 μM) abolished the effect of PBP1B on HCC cell proliferation (**l**) and colony formation (**m**). *n* = 3 biologically independent samples. **n**, Effect of *K. pneumoniae* on TLR4 expression in liver tissues of both germ-free and SPF mice with or without DEN treatment by IHC staining. In **b,c**, **j–m**, data are presented as mean ± s.e.m. Each data point in bar plots represents one mouse. Cell proliferation was analysed using two-way ANOVA. In **b,c,j,k,m**, comparisons between two groups were analysed using Student's *t*-test. Unless otherwise stated, statistical significance was calculated using one-way ANOVA. Adjustments were made for multiple comparisons.

axis (Supplementary Fig. 17). Targeting *K. pneumoniae* represents a strategy for HCC prevention and treatment. The DEN-induced HCC mouse model used in this study is not a perfect tumour model and probably does not reflect human disease very well.

Methods

Ethics oversight
Written informed consent was obtained for all human samples and this study was approved by the Ethics Committee of The First Affiliated Hospital of Sun Yat-sen University (ID No. [2024]141 and [2020]361). Corresponding compensation was provided to participants.

All experiments were approved by the Animal Experimentation Ethics Committee of The First Affiliated Hospital of Sun Yat-sen University (ID No. [2021]506, [2023]361, [2024]141) or Shenzhen Jingtuo Biotechnology (ID No. [2023]51), which required a maximum tumour volume not exceeding 2,000 mm³, maximum diameter not exceeding 15 mm and tumour weight not exceeding 5% of body weight. The maximum tumour size and tumour burden in this study did not exceed this limit.

Human samples collection
As shown in Supplementary Table 1, we collected stool from healthy donors (*N* = 20), individuals with LC (*N* = 20) and individuals with HCC (*N* = 20). In addition, we also collected stool from another batch of healthy donors (*N* = 5) and individuals with HCC (*N* = 5) (Supplementary Table 2) at The First Affiliated Hospital of Sun Yat-sen University. The exclusion criteria were as follows: (1) use of antibiotics within the past 3 months, (2) had received previous cancer treatment, (3) had a history of other cancers and (4) presence of intrahepatic cholangiocarcinoma and a history of gastrointestinal surgeries. Fresh faecal samples were collected using sterile stool collection tubes, placed in anaerobic conditions created by the AnaeroPack-Anaero (C-35, Mitsubishi Gas Chemical) and transported to the laboratory on ice. Stool samples were suspended in sterile PBS in an anaerobic glove box (COY-8300400, Coy Laboratory) and the suspension was filtered using a 40-μm cell strainer and centrifuged at 100 *g* for 1 min to remove debris. Supernatant was then centrifuged at 10,000 *g* for 8 min, and the bacterial pellet was suspended with 25% sterile glycerol and stored at −80 °C. We also collected stool samples from individuals with HCC (*N* = 24) with overall survival and progression-free survival data (Supplementary Table 3).

Fresh LC tissues (*N* = 15) and HCC tumours tissues (*N* = 54) were collected for live bacterial culture, 16S rRNA sequencing and wax block embedding (Supplementary Table 4) from patients who underwent surgery at The First Affiliated Hospital of Sun Yat-sen University.

Mice
Animals used in experiments were gender and age matched. SPF BALB/c and C57BL/6J mice were purchased from GemPharmatech and raised at Jingtuo Biotechnology. Germ-free male BALB/c mice were bred and housed at the Germ-Free Mouse Research Facility, The First Affiliated Hospital of Sun Yat-sen University or Shenzhen Jingtuo Biotechnology. Mice were raised in SPF or sterile facilities, following a cycle of 12 h light and 12 h dark conditions. Food (for SPF mice: 1010058, Jiangsu Xietong; for germ-free mice: 1019018, Jiangsu Xietong) and sterile water were provided ad libitum. Mice were randomly assigned to various experimental groups and experimental treatments. No statistical methods were used to predetermine sample sizes, but our sample sizes are similar to those reported in previous publications[6]. All mice were euthanized by pentobarbital sodium and cervical dislocation.

Bacteria
K. pneumoniae (isolated from tumour tissues of patients with HCC in this study), *E. coli* (used in Fig. 4a, isolated from tumour tissues of patients with HCC in this study), *B. thetaiotaomicron* (isolated from tumour tissues of HCC-FMT-treated mice in this study), *P. mirabilis* (isolated from tumour tissues of HCC-FMT-treated mice in this study), *Enterobacter hormaechei* (isolated from tumour tissues of HCC-FMT-treated mice in this study), *E. coli* MG1655 (700926, American Type Culture Collection (ATCC)) and *K. oxytoca* (DSM5175, DSMZ) were all cultured in brain heart infusion (BHI) broth (024053, Huanan Microbial) at 37 °C under aerobic/anaerobic conditions.

Cell lines
Both human HCC cell lines Hep3B (HB-8064, ATCC), Huh7 (01042712, Sigma-Aldrich) and normal colonic epithelial cells NCM460 (NCM460D, Incell) cells were cultured in Dulbecco's modified Eagle's medium (DMEM) (11965092, Thermo Fisher) supplemented with 10% fetal bovine serum (FBS) and 1% penicillin/streptomycin at 37 °C in a humidified atmosphere of 5% CO_2.

Germ-free and SPF mouse models
For germ-free mice without DEN treatment, 8-week-old male germ-free BALB/c mice were selected for FMT or bacterial gavage. For SPF mice without DEN treatment, 8-week-old male SPF BALB/c or C57BL/6J mice were selected for FMT or bacterial gavage. The number of mice in each group is shown in the figure legends.

For germ-free mice with DEN treatment, 14-day-old male germ-free BALB/c mice were selected and given 25 mg kg⁻¹ DEN (N0756, Sigma-Aldrich) intraperitoneal injection. For SPF mice with

DEN treatment, 14-day-old male SPF BALB/c or C57BL/6J mice were selected and given 25 mg kg^{-1} DEN intraperitoneal injection. The number of mice in each group is shown in the figure legends. FMT or other bacterial (as shown in figure legends) gavage only started when mice reached adulthood at 8 weeks of age.

At the end point, mice were anaesthetized with sodium pentobarbital intraperitoneally. Tumour number and size in the liver were recorded. Tumour volume was measured by length (*a*) and width (*b*) using a digital caliper and calculated as tumour volume = $ab^2/2$. Tumour burden was the summation of tumour volumes of each liver. Liver and colon tissues were collected in 4% paraformaldehyde, 2% glutaraldehyde or snap-frozen. For bacterial culture and 16S rRNA sequencing, fresh liver tissues were collected in the biosafety cabinet. Liver histology was assessed by H&E staining (BL735B, Biosharp) of paraffin-embedded sections. Fresh liver and colon tissues were collected for flow cytometry. Liver histology was evaluated by a pathologist, B.L., blinded to the treatment conditions.

Bacterial culture from liver tissue and strain identification
Fresh liver tissues from mice, and patients with LC or HCC were collected in sterile tubes with BHI broth under aerobic and anaerobic conditions. Tissues were washed six times with sterile phosphate-buffered saline (PBS) and chopped into pieces. Tissue pieces were homogenized using TissueLyser II (85300, QIAGEN), and 100 μl tissue homogenate was directly spread onto different agar plates including blood agar plates, chocolate agar plates, MacConkey agar plates and Columbia blood agar plates in both anaerobic and aerobic conditions at 37 °C. Colony-forming units (c.f.u.) per mg tissue was counted. Full-length 16S rRNA sequencing or microbial mass spectrometry (MALDI Biotyper smart, Bruker) was used for strain identification.

Whole-genome sequencing and assemblies of *K. pneumoniae*
Genomic DNA was extracted from the isolated *K. pneumoniae* using the Tris-EDTA-NaCl buffer extraction method. The collected DNA was detected using agarose gel electrophoresis and quantified using Qubit. After quality control, the high-quality genomic DNA was subjected to sequencing library building and the genome of *K. pneumoniae* was sequenced using single-molecule, real-time technology (Novogene Bioinformatics). Low-quality reads were filtered using SMRT Link v.8.0 and the filtered reads were assembled using the software Canu to generate one contig without gaps. PacBio long-read sequencing of our *K. pneumoniae* isolate from HCC tissues revealed the absence of virulence factors associated with liver abscess (for example, *peg-344*, *iroB*, *iucA*, *rmpA* and *rmpA2* encoding proteins) (Supplementary Table 6), which might explain why it colonizes in HCC without causing abscesses.

16S rRNA sequencing of liver tissues and stool samples
Liver tissues from mice and humans were collected in a biosafety cabinet for 16S rRNA sequencing. Liver tissues were disrupted by bead beating after digestion with mutanolysin and lysozyme. DNA extraction was performed with the QIAamp DNA mini kit (51304, QIAGEN). DNA of mice and human faecal bacteria were extracted using the Quick-DNA Faecal/Soil Microbe Miniprep kit (D6010, Zymo). DNA library preparation and 16S rRNA gene sequencing were performed on an Illumina NovaSeq 6000 platform by Gene Denovo. The V3–V4 region of bacterial 16S rRNA was PCR amplified using 16S primers 341F (5′-CCTAYGGGRBGCASCAG-3′) and 806R (5′-GGACTACNNGGGTATCTAAT-3′), with no template DNA reaction as negative control. Sequencing libraries were generated using the TruSeq DNA PCR-Free Sample Preparation kit (FC-121-3001, Illumina) and sequenced on an Illumina NovaSeq platform. After quality control, paired-end reads were overlapped to assemble the final sequences (overlap region >10 bp, mismatch ratio <0.2). Chimaera tags were filtered out using the Gold database by UCHIME (v.4.2.40).

Operational taxonomic unit (OTU) analysis was performed using the Uparse package (v.7.0.1001) with 97% sequence identity. Each OTU was taxonomically assigned to the silva database using the RDP classifier. OTUs with relative abundance values >0.001% in at least one sample were retained.

Shotgun metagenomic sequencing
DNA of mouse faecal bacteria was extracted using the Quick-DNA Faecal/Soil Microbe Miniprep kit (D6010, Zymo). Shotgun metagenomic sequencing of faecal DNA was performed on an Illumina NovaSeq 6000 platform by Gene Denovo. Taxonomy was assigned to metagenomic reads using *k*-mer-based algorithms implemented in the Kraken taxonomic annotation pipeline. A standard database comprising 13,844 bacterial genomes from NCBI was built using the Jellyfish programme by counting distinct 31-mers. Each *k*-mer in a read was mapped to the lowest common ancestor of all reference genomes with exact *k*-mer matches. Each query was thereafter classified to a taxon, with the highest total hits of *k*-mers matched by pruning the general taxonomic trees affiliated with mapped genomes. Final metagenomic read counts were normalized with the cumulative sum scaling method using metagenome Seq R/Bioconductor.

K. pneumoniae correlates with prognosis of patients with HCC
K. pneumoniae relative abundance in stool samples from individuals with HCC (*N* = 24) was detected using qPCR assay (Forward: 5′-CGATG CTACTTATCCCGACA-3′; Reverse: 5′-AGCCGGTTGAGACGTAAAC-3′), and correlation analysis between *K. pneumoniae* relative abundance and overall survival or progression-free survival was performed.

IHC
IHC on paraffin-embedded tissues was used for the detection of PCNA (1:5,000), Ki-67 (1:400), TLR4 (1:5,000), E-cad (1:200), CLDN1 (1:200), CLDN3 (1:100), α-SMA (1:1,000), desmin (1:2,000), fibronectin (1:2,000), COLIV (1:500), LPS (1:200) and LTA (1:400) (antibodies listed in Supplementary Table 5). Quantitative analysis was performed using ImageJ (v.1.51, National Institutes of Health (NIH)).

Sirius red staining
Sirius red staining was conducted using the commercial kit (BP-DL030, Nanjing SenBeiJia) according to manufacturer instructions to evaluate collagen fibre content in liver tissues. Quantitative analysis was performed using ImageJ (v.1.51, NIH).

Masson's trichrome staining
Masson's trichrome staining was conducted using the commercial kit (BP-DL022, Nanjing SenBeiJia) according to manufacturer instructions to evaluate collagen fibre content in colon tissues. Quantitative analysis was performed using ImageJ (v.1.51, NIH).

Western blot
Total protein was extracted using Minute Total Protein Extraction Kit for Animal Cultured Cells/Tissues (SD-001, Invent Biotechnologies). Protein levels were measured using the BCA Protein Assay kit (ZJ101, Shanghai Epizyme). Proteins (30 μg) were separated using 12% gel and transferred onto PVDF membranes (SEQ85R, Merck Millipore). Membranes were incubated with primary antibody (1:1,000) overnight at 4 °C and then secondary antibody (1:5,000) (HRP-linked anti-mouse IgG 7076, HRP-linked anti-rabbit IgG 7074, Cell Signaling Technology) for 1 h. Proteins were visualized using a chemiluminescence reagent (SQ201, Shanghai Epizyme). β-actin was used as the total protein loading control. Antibodies used are listed in Supplementary Table 5.

FITC-dextran permeability assay
Mice were gavaged with 500 kDa FITC-dextran (FD500S, Sigma-Aldrich) after overnight fasting. Blood samples were collected from the tail vein

at 4 h post administration. FITC-dextran in the plasma was measured in a spectrophotometer (Varioskan LUX, Thermo Scientific).

Gelatinase activity assay

The gelatin hydrolysis activity of faecal supernatant with various treatments or KPCM were detected using a gelatin biochemical identification tube (075310, HuanKai Microbial) and a gelatin zymography assay kit (RTD6143, Real-Times Biotechnology). MMP-2 and MMP-9 activities were detected using the MMP Activity Assay kit (ab112146, Abcam).

Effects of MMP-2/9 protein on gut barrier markers in vitro

MMP-2 (HY-P70268, MCE) and MMP-9 (HY-P70145, MCE) were used at 0.01 μg ml^{-1} and co-cultured with NCM460 cells for 3 days. Then, western blot assay was conducted to evaluate the effects of MMP-2/9 protein on gut barrier markers COLIV, fibronectin, E-cad and ZO-1. Antibodies used are listed in Supplementary Table 5.

FISH assay

Paraffin-embedded liver and colon sections were used for FISH assay using the Bacterial DNA FISH Assay kit (D-0015, FOCO Biology). Hybridization was performed at 37 °C for 2 days with a universal 16S rRNA probe EUB338 (5′-GCTGCCTCCCGTAGGAGT-3′, with a Cy3 label), E. coli probe (5′-GCATAAGCGTCGCTGCCG-3′, with a Cy3 label) or K. pneumoniae probe (5′-CCTACACACCAGCGTGCC-3′, with a Cy3 label) at 0.25 μM in hybridization buffer. After washing three times in wash buffer, slides were rinsed with sterile double-distilled water, air-dried in the dark and mounted in mounting medium with DAPI (ab104139, Abcam). Microscopic observations were performed using a fluorescence microscope (BX63F, Olympus).

RT² profiler qPCR array

Total RNA was isolated from liver and colon tissues using TRIzol reagent (15596026, Thermo Fisher) and reverse transcribed using RT² First Strand kit (330401, QIAGEN). RT² Profiler PCR Array Mouse Cancer Pathway Finder (PAMM-033ZA-6, QIAGEN) or RT² Profiler PCR Array Mouse Inflammatory Response and Autoimmunity (PAMM-077Z, QIAGEN) was used for qPCR analysis.

HCC patient-derived organoid culture and experiment

Organoids from patients with HCC (668T) were provided by N. Wong (The Chinese University of Hong Kong), embedded into Matrigel (356231, Corning) and cultured in AIM-V medium (12055083, Thermo Fisher) supplemented with 10% FBS, 1% penicillin/streptomycin, 1% L-glutamine (25030081, Thermo Fisher), MEM non-essential amino acids solution (11140050, Thermo Fisher) and insulin-transferrin-selenium (41400045, Thermo Fisher). Culture medium was changed every 3 days. After 10 days, HCC organoids were digested using TrypLE Express (12604013, Thermo Fisher) and collected for experiments. To investigate the effects of candidate bacteria or proteins on organoid growth, images were captured and the diameter of organoids in each random field was measured using ImageJ (v.1.51, NIH) after treatment for 5 days. The effect of PBP1B (0.05 μM) on the growth of HCC patient-derived organoids was also investigated as stated above.

Flow cytometry analysis of immune cells

Multicolour flow cytometry was performed to study the immune cell types in liver and colon tissues. Single-cell suspensions of liver and colon tissues were prepared with the Liver Dissociation kit (130-105-807, Miltenyi Biotec) or the Lamina Propria Dissociation kit (130-097-410, Miltenyi Biotec), respectively. For surface staining, cells were incubated with Fc block antibody purified rat anti-mouse CD16/CD32 (1:100) (553142, BD Biosciences) for 30 min. Then, cells were stained with the following antibodies: CD45 (1:100; 157213, Biolegend), FVS510 (1:100; 564406, BD Biosciences), CD3 (1:100; 100330, Biolegend), CD4 (1:100; 100434, Biolegend), CD11b (1:100; 101216, Biolegend), MHC II

(1:100; 107622, Biolegend) or Ly-6C (1:100; 560525, BD Biosciences). For intracellular markers, cells were stimulated for 8 h in DMEM with leucocyte activation cocktail. Then, cells were fixed and permeabilized with BD GolgiPlug kit (550583, BD Bioscience) and then stained with intracellular cytokine IFNγ (1:100; 557649, BD Bioscience), IL-4 (1:100; 564005, BD Bioscience) and IL-17 (1:100; 563354, BD Bioscience) antibodies. Flow cytometry was performed on an Attune NxT Acoustic Focusing cytometer (ThermoFisher). Gating strategy for flow cytometry is shown in Supplementary Fig. 16a. Antibodies used are listed in Supplementary Table 5.

THP-1-induced macrophage in vitro and co-culture experiment

THP-1 monocyte cells (TIB-202, ATCC) were cultured in RPMI 1640 medium (11875093, Gibco). THP-1 cells were differentiated into macrophages by 3 days incubation with 150 nM phorbol ester (P8139, Sigma), followed by morphological observation and flow cytometry to evaluate CD14 (1:100; 367140, Biolegend) expression. THP-1-induced macrophages were then co-cultured with K. pneumoniae (multiplicity of infection (MOI) = 10) for 2 h and subsequently cultured for another 3 days. After that, the cell suspension was centrifuged at 10,000g for 10 min at 4 °C to collect the supernatant for gelatinase activity assay. The gating strategy for flow cytometry is shown in Supplementary Fig. 16b. Antibodies used are listed in Supplementary Table 5.

Colon macrophage depletion mouse model

We used the macrophage depletion reagent Clodrosome (CLD-8909, Encapsula NanoSciences) according to manufacturer instructions to deplete colon macrophages. After killing, macrophages in colon were detected by flow cytometry. Macrophages in colon were marked as CD45$^+$ MHC II$^+$ CD11b$^+$ Ly6C$^-$. The gating strategy for flow cytometry is shown in Supplementary Fig. 16c. Antibodies used are listed in Supplementary Table 5.

Live K. pneumoniae attachment to HCC cells assay

Live K. pneumoniae (MOI = 10) was suspended in DMEM medium supplemented with 10% FBS and co-cultured with Hep3B or Huh7 cells for 2 h in 6-well plates. Then, cells were washed with warm PBS six times and scraped off from plates. The cells were collected and stripped in BHI agar for culture.

SEM and TEM assay of K. pneumoniae and HCC cell attachment

Hep3B or Huh7 cells (1 × 10^6) were seeded in sterile coverslips and co-cultured with K. pneumoniae (MOI = 10) for 2 h. Next, cells were washed with PBS three times and fixed with 2.5% glutaraldehyde fixative at 4 °C overnight. The fixed coverslips were washed with Sorensen's phosphate buffer three times and fixed in 1% osmium tetroxide for 2 h, followed by rinsing with double-distilled water. After dehydration and coating with gold-palladium, specimens were examined using a Cold Field Scanning Electron Microscope (SU8010, Hitachi). Hep3B or Huh7 cells (1 × 10^6) were seeded in 6-well plates and co-cultured with K. pneumoniae for 4 h (MOI = 10), followed by fixation in 2.5% glutaraldehyde. Fixed samples were further fixed in 2% osmium tetroxide and dehydrated with a gradient of ethanol and propylene oxide. Samples were then embedded, sectioned and stained with 3% uranyl acetate and lead citrate. Pictures were taken using an HT7700 TEM (Hitachi).

Cell membrane protein extraction

Hep3B or Huh7 cells were extracted with 0.5 ml ice-cold lysis buffer (150 mM NaCl, 10 mM Tris-HCl (pH 7.4), 1 mM EDTA, 1 mM EGTA (pH 8.0), 0.2 mM sodium orthovanadate, 0.2 mM phenylmethylsulfonylfluoride, 1% Triton X-100, 0.5% NP-40) for 1 h at 4 °C, followed by sonication on ice for 15 min. The cell suspension was centrifuged at 10,000 g for 10 min at 4 °C to collect the supernatant, which was then used as the cell membrane protein lysate.

Biotin pull-down assay and silver staining

Biotin pulldown was performed as previously described[35]. In brief, Hep3B or Huh7 cells were labelled with 1 mM EZ-Link Sulfo-NHS-LC-Biotin (21338, Thermo Scientific) at 4 °C for 2 h, and then incubated with *K. pneumoniae* surface membrane proteins overnight at 4 °C, followed by incubation with streptavidin magnetic beads for 6 h at 4 °C. As a negative control, streptavidin agarose resin was incubated with non-biotinylated Hep3B or Huh7 surface proteins. Finally, the beads were washed with PBST (PBS with 0.1% Tween 20) three times, boiled with SDS–PAGE gel loading buffer and centrifuged. Eluted proteins were subjected to SDS–PAGE and visualized by silver staining using the Pierce Silver Stain for Mass Spectrometry kit (24600, Thermo Scientific). Corresponding bands of gels were identified by mass spectrometry.

Expression and purification of PBP1B protein with or without GST tag

To generate recombinant GST–PBP1B protein, the non-transmembrane domain of PBP1B (accession: A0A086I8Y5) was cloned into the pGEX-6P-1 vector and transformed into *E. coli* BL21 (DE3). Transformed *E. coli* was grown in ampicillin-supplemented LB broth at 37 °C. When optical density reached 1.0, 0.5 mM IPTG (HY-15921, MCE) was added to induce protein synthesis at 20 °C overnight. Bacterial pellets were collected and suspended in PBS-basic lysis buffer (50 mM NaH_2PO_4, 150 mM NaCl, pH 7.2, 10 mg ml^{-1} lysozyme and proteinase inhibitors). After centrifugation at 10,000 *g* for 30 min, GST–PBP1B (113 kDa) was purified from the supernatant using GST-tag Protein Purification kit (P2262, Beyotime). GST–PBP1B was incubated with PreScission protease (27084301, Cytiva) to obtain PBP1B without the GST tag (87 kDa).

GST pull-down assay

To perform the GST pulldown, Hep3B or Huh7 membrane proteins were incubated with or without recombinant GST–PBP1B protein overnight at 4 °C, followed by addition of glutathione magnetic agarose beads (HY-K0234, MCE) for another 4 h at 4 °C. The beads were then washed and boiled with SDS–PAGE gel loading buffer. Eluted proteins were separated by SDS–PAGE. Then, gel was analysed by silver staining, followed by mass spectrometry analysis of target bands, or western blot assay. Antibodies used are listed in Supplementary Table 5.

Co-immunoprecipitation

For co-immunoprecipitation of TLR4, anti-TLR4 antibody (1:100) and Hep3B or Huh7 cell membrane protein were incubated with or without recombinant GST-PBP1B overnight at 4 °C. Mouse IgG (1:100) served as the negative control. Dynabeads Protein G magnetic beads (10004D, Invitrogen) were then added and incubated for another 4 h. The beads were washed and boiled with loading buffer. Boiled samples were subjected to SDS–PAGE and immunoblotted with anti-TLR4 (1:1,000) or anti-GST (1:5,000) (2624, Cell Signaling Technology). Antibodies used are listed in Supplementary Table 5.

SPR

Binding affinity between PBP1B and TLR4 was evaluated by SPR using Biacore T200 (GE Healthcare). TLR4 human recombinant protein (HY-P73586, MCE) was immobilized on a Series S Sensor Chip CM5 (29149603, GE Healthcare) using an amine coupling kit (BR-1000-50, GE Healthcare) with a flow rate of 10 µl min^{-1}, resulting in a final ligand coupling of ~180 response units. Different concentrations of PBP1B (100, 50, 25, 12.5, 6.25, 3.125 and 0 nM) diluted using an analyte buffer were injected at a flow rate of 30 µl min^{-1} for an association phase of 120 s, followed by a 300-s dissociation. The association and dissociation processes were all handled in the analyte buffer. We repeated 7 cycles of analysis according to analyte concentration in ascending order. After each cycle of interaction analysis, the sensor chip surface was

regenerated completely with 10 mM glycine-HCl as injection buffer at a flow rate of 30 µl min^{-1} for 30 s to remove the analyte, then the injection and regeneration steps were repeated for the next concentration cycle of the analyte PBP1B. The Biacore T200 Evaluation Software v.2.0 was used to determine the binding affinity.

Molecular docking analysis

Molecular docking analysis was performed to determine receptor–ligand interactions. The three-dimensional structures of PBP1B (accession: A0A086I8Y5) and TLR4 (O00206) were predicted using AlphaFold. Protein was pretreated using Discovery Studio software to remove water molecules, hydrogenation and ions. The primary ligand was extracted from the structure and the treated protein was visualized using Pymol. The 2D ligand–protein interaction diagrams and hydrophobic interactions were constructed using the software LigPlus.

Alcian blue staining

Paraffin-embedded colonic sections were stained using the Alcian Blue Stain kit (S0134, Bioss). Alcian blue staining-positive areas were analysed using ImageJ (v.1.51, NIH).

TEM assay of colon and liver tissues

Ultra-thin sections of colon and liver tissues were prepared and examined using an HT7700 TEM (Hitachi), then photographed for analysis.

K. pneumoniae quantification by qPCR

Stool DNA was prepared using the Quick-DNA Faecal/Soil Microbe kit (D6110, Zymo), while bacterial DNA from liver tissues was prepared using the QIAamp DNA Mini kit (51306, QIAGEN) combined with RNase A (R6513, Sigma-Aldrich) and lysozyme (L6876, Sigma-Aldrich). Quantification of *K. pneumoniae* was performed using the *K. pneumoniae*-EASY Genesig kit (Z-Path-*K. pneumoniae*-standard, Primer Design) and Oasig lyophilised 2× qPCR Master Mix (Z-oasig-standard-150, Primer Design) in an Applied Biosystems Real-Time PCR System (QuantStudio 5, Thermo Fisher).

Colony formation and cell proliferation

KPCM was prepared by culture in BHI broth for 2 days, followed by bacterial removal by centrifugation and filtration with a 0.22-µm filter. Pasteurized *K. pneumoniae* was prepared by incubating live *K. pneumoniae* at 70 °C for 30 min. For colony formation, cells were seeded on 6-well plates (1,000 cells per well). KPCM (5% or 10%) or pasteurized *K. pneumoniae* (MOI = 10) treatment was performed for 3 h day^{-1}, then the medium was replaced with MEM or DMEM containing 10% FBS, 1% penicillin/streptomycin and 20 mg ml^{-1} gentamycin. The procedure was repeated for 14 days and colonies were stained with 0.5% crystal violet. For the cell proliferation assay, cells were seeded into 96-well plates (1,000 cells per well), followed by live *K. pneumoniae* or culture supernatant treatment. At different time intervals, cell viability was determined using the MTT (475989, Sigma-Aldrich) assay and measured under an optical density of 570 nm using a spectrophotometer. In addition, PBP1B (0.05 µM) effects on HCC cell proliferation and colony formation were also assessed as stated above.

Bacterial fluorescence tracing experiment

To label *K. pneumoniae* and *E. coli* MG1655, bacteria were cultured in BHI containing 100 µmol l^{-1} Cy5.5-ᴅ-Lys at 37 °C for 48 h. Bacterial suspension was collected by centrifugation and washed with PBS six times. Labelling was determined using a fluorescence microscope (BX63F, Olympus). To trace bacteria in vivo, labelled bacteria were gavaged to germ-free mice and fluorescence detection was performed before bacterial gavage and 8 h after gavage using the in vivo imaging system (IVIS Lumina III, Perkin Elmer). Hepatic fluorescence detection was also conducted after collecting the liver.

TLR4i treatment in vitro and in vivo

For in vitro treatment, the TLR4i TLR4-IN-C34 (HY-107575, MCE) was used at 30 μM, while mice received TLR4-IN-C34 (1 mg kg^{-1}) gavaged daily in vivo.

Colonization resistance challenge of *K. pneumoniae* in vivo

K. oxytoca was used to cause colonization resistance to *K. pneumoniae* in the gut of germ-free mice. Mice were gavaged with 1×10^8 c.f.u. of *K. oxytoca* diluted in 200 μl PBS. After 3 days of precolonization, mice were gavaged with 1×10^8 c.f.u. of *K. pneumoniae*. This process was conducted once a week. For mice receiving only *K. oxytoca* treatment, mice were given 1×10^8 c.f.u. of *K. oxytoca* gavaged once a week.

Statistical analysis

No animals or data points were excluded from the analyses. Data collection and analysis were not performed blind to the conditions of the experiments. Data distribution was assumed to be normal but this was not formally tested. Measurements were taken from distinct samples. All in vitro experiments were repeated three times as three independent experiments unless otherwise stated. For in vitro experiments, all attempts at replication were successful. For in vivo experiments, all experiments were successful without replication. Data are expressed as mean ± s.e.m. for both in vivo and in vitro experiments. Comparison between two groups was performed using Student's *t*-test. One-way ANOVA was used to compare differences among multiple groups. Differences in cell proliferation and MMP activity were determined using two-way ANOVA. Fisher's exact test was used to evaluate the proportional difference in categorical variables between groups. Simple linear regression analysis was conducted to characterize the correlation between two variables. Correlation coefficient, *r*, was calculated using Goodness of Fit test. All statistical analyses were conducted using GraphPad Prism v.10.3.1. Flow cytometry data were analysed with the FlowJo v.10.9.0 software. *P* value < 0.05 indicates statistical significance.

Reagent and resource sharing

Further information and requests for resources, biological materials and reagents should be directed to and will be fulfilled by the lead contact, J.Y.

Reporting summary

Further information on research design is available in the Nature Portfolio Reporting Summary linked to this article.

Data availability

All datasets generated and/or analysed during the study are available. All related raw data have been deposited to public datasets with accession numbers. Whole-genome sequencing data of *Klebsiella pneumoniae* reported in this study have been deposited at the Genome Sequence Archive (GSA) of the China National Center for Bioinformation (CNCB) under accession number CRA019172. 16S rRNA sequencing data of liver tissues and stools from patients with LC and HCC have been deposited at the GSA of CNCB under accession numbers CRA019234 and CRA019232, respectively. 16S rRNA sequencing data and metagenomic sequencing sequencing data of mice faeces have been deposited at the GSA of CNCB under accession numbers CRA019231 and CRA019388, respectively. Source data are provided with this paper.

References

1. Sung, H. et al. Global cancer statistics 2020: GLOBOCAN estimates of incidence and mortality worldwide for 36 cancers in 185 countries. *CA Cancer J. Clin.* **71**, 209–249 (2021).
2. Fujiwara, N., Friedman, S. L., Goossens, N. & Hoshida, Y. Risk factors and prevention of hepatocellular carcinoma in the era of precision medicine. *J. Hepatol.* **68**, 526–549 (2018).
3. Behary, J. et al. Gut microbiota impact on the peripheral immune response in non-alcoholic fatty liver disease related hepatocellular carcinoma. *Nat. Commun.* **12**, 187 (2021).
4. Nejman, D. et al. The human tumor microbiome is composed of tumor type-specific intracellular bacteria. *Science* **368**, 973–980 (2020).
5. Dejea, C. M. et al. Patients with familial adenomatous polyposis harbor colonic biofilms containing tumorigenic bacteria. *Science* **359**, 592–597 (2018).
6. Iida, N. et al. Chronic liver disease enables gut *Enterococcus faecalis* colonization to promote liver carcinogenesis. *Nat. Cancer* **2**, 1039–1054 (2021).
7. Fu, A. et al. Tumor-resident intracellular microbiota promotes metastatic colonization in breast cancer. *Cell* **185**, 1356–1372 (2022).
8. Dohlman, A. B. et al. A pan-cancer mycobiome analysis reveals fungal involvement in gastrointestinal and lung tumors. *Cell* **185**, 3807–3822 (2022).
9. Pabst, O. et al. Gut–liver axis: barriers and functional circuits. *Nat. Rev. Gastroenterol. Hepatol.* **20**, 447–461 (2023).
10. Schnabl, B. & Brenner, D. A. Interactions between the intestinal microbiome and liver diseases. *Gastroenterology* **146**, 1513–1524 (2014).
11. Manfredo Vieira, S. et al. Translocation of a gut pathobiont drives autoimmunity in mice and humans. *Science* **359**, 1156–1161 (2018).
12. Dapito, D. H. et al. Promotion of hepatocellular carcinoma by the intestinal microbiota and TLR4. *Cancer Cell* **21**, 504–516 (2012).
13. Albillos, A., de Gottardi, A. & Rescigno, M. The gut-liver axis in liver disease: pathophysiological basis for therapy. *J. Hepatol.* **72**, 558–577 (2020).
14. McCawley, L. J. & Matrisian, L. M. Matrix metalloproteinases: they're not just for matrix anymore! *Curr. Opin. Cell Biol.* **13**, 534–540 (2001).
15. Kirkegaard, T., Hansen, A., Bruun, E. & Brynskov, J. Expression and localisation of matrix metalloproteinases and their natural inhibitors in fistulae of patients with Crohn's disease. *Gut* **53**, 701–709 (2004).
16. Tan, T. K. et al. Macrophage matrix metalloproteinase-9 mediates epithelial-mesenchymal transition in vitro in murine renal tubular cells. *Am. J. Pathol.* **176**, 1256–1270 (2010).
17. Bai, X. et al. Changes in MMP-2, MMP-9, inflammation, blood coagulation and intestinal mucosal permeability in patients with active ulcerative colitis. *Exp. Ther. Med.* **20**, 269–274 (2020).
18. Osbelt, L. et al. *Klebsiella oxytoca* causes colonization resistance against multidrug-resistant *K. pneumoniae* in the gut via cooperative carbohydrate competition. *Cell Host Microbe* **29**, 1663–1679 (2021).
19. Osbelt, L. et al. *Klebsiella oxytoca* inhibits *Salmonella* infection through multiple microbiota-context-dependent mechanisms. *Nat. Microbiol.* **9**, 1792–1811 (2024).
20. Okuda, K. Hepatocellular carcinoma: recent progress. *Hepatology* **15**, 948–963 (1992).
21. Brescia, P. & Rescigno, M. The gut vascular barrier: a new player in the gut-liver-brain axis. *Trends Mol. Med.* **27**, 844–855 (2021).
22. Zitta, K. et al. Serum from patients undergoing remote ischemic preconditioning protects cultured human intestinal cells from hypoxia-induced damage: involvement of matrixmetalloproteinase-2 and-9. *Mol. Med.* **18**, 29–37 (2012).
23. Jakubowska, K. et al. Expressions of matrix metalloproteinases (MMP-2, MMP-7, and MMP-9) and their inhibitors (TIMP-1, TIMP-2) in inflammatory bowel diseases. *Gastroenterol. Res. Pract.* **2016**, 2456179 (2016).
24. Rodrigues, D. M. et al. Matrix metalloproteinase 9 contributes to gut microbe homeostasis in a model of infectious colitis. *BMC Microbiol.* **12**, 105 (2012).

25. Spadoni, I. et al. A gut-vascular barrier controls the systemic dissemination of bacteria. *Science* **350**, 830–834 (2015).

26. Ren, Z. et al. Gut microbiome analysis as a tool towards targeted non-invasive biomarkers for early hepatocellular carcinoma. *Gut* **68**, 1014–1023 (2019).

27. Nakamoto, N. et al. Gut pathobionts underlie intestinal barrier dysfunction and liver T helper 17 cell immune response in primary sclerosing cholangitis. *Nat. Microbiol.* **4**, 492–503 (2019).

28. Yuan, J. et al. Fatty liver disease caused by high-alcohol-producing *Klebsiella pneumoniae*. *Cell Metab.* **30**, 675–688 (2019).

29. Atarashi, K. et al. Ectopic colonization of oral bacteria in the intestine drives TH1 cell induction and inflammation. *Science* **358**, 359–365 (2017).

30. Ganaway, J. R. in *The Biology of the Guinea Pig* (eds Wagner. J. E. & Manning, P. J.) 121–135 (Elsevier, 1976).

31. Wagner, K. A., Hartmann, F. A. & Trepanier, L. A. Bacterial culture results from liver, gallbladder, or bile in 248 dogs and cats evaluated for hepatobiliary disease: 1998–2003. *J. Vet. Intern. Med.* **21**, 417–424 (2007).

32. Lederman, E. R. & Crum, N. F. Pyogenic liver abscess with a focus on *Klebsiella pneumoniae* as a primary pathogen: an emerging disease with unique clinical characteristics. *Am. J. Gastroenterol.* **100**, 322–331 (2005).

33. Niño, J. L. G. et al. Effect of the intratumoral microbiota on spatial and cellular heterogeneity in cancer. *Nature* **611**, 810–817 (2022).

34. Federici, S. et al. Targeted suppression of human IBD-associated gut microbiota commensals by phage consortia for treatment of intestinal inflammation. *Cell* **185**, 2879–2898 (2022).

35. Long, X. et al. *Peptostreptococcus anaerobius* promotes colorectal carcinogenesis and modulates tumour immunity. *Nat. Microbiol.* **4**, 2319–2330 (2019).

Acknowledgements

Author contributions

Competing interests

The authors declare no competing interests.

Additional information

Extended data is available for this paper at https://doi.org/10.1038/s41564-024-01890-9.

Supplementary information The online version contains supplementary material available at https://doi.org/10.1038/s41564-024-01890-9.

Correspondence and requests for materials should be addressed to Jun Yu.

Peer review information *Nature Microbiology* thanks Tim Greten and the other, anonymous, reviewer(s) for their contribution to the peer review of this work.

Reprints and permissions information is available at www.nature.com/reprints.

Publisher's note Springer Nature remains neutral with regard to jurisdictional claims in published maps and institutional affiliations.

[1]Department of Liver Surgery, Center of Hepato-Pancreato-Biliary Surgery, The First Affiliated Hospital, Sun Yat-sen University, Guangzhou, China. [2]Institute of Digestive Disease and The Department of Medicine and Therapeutics, State Key Laboratory of Digestive Disease, Li Ka Shing Institute of Health Sciences, CUHK Shenzhen Research Institute, The Chinese University of Hong Kong, Hong Kong, China. [3]Institute of Precision Medicine, The First Affiliated Hospital, Sun Yat-sen University, Guangzhou, China. [4]Organ Transplant Center, The First Affiliated Hospital, Sun Yat-sen University, Guangzhou, China. [5]Department of Oncology, The First Affiliated Hospital, Sun Yat-sen University, Guangzhou, China. [6]Department of Pathology, The First Affiliated Hospital, Sun Yat-sen University, Guangzhou, China. [7]Lee Kong Chian School of Medicine, Nanyang Technological University, Singapore, Singapore. [8]These authors contributed equally: Xueliang Wang, Yi Fang, Wei Liang, Yuhong Cai. ✉e-mail: junyu@cuhk.edu.hk
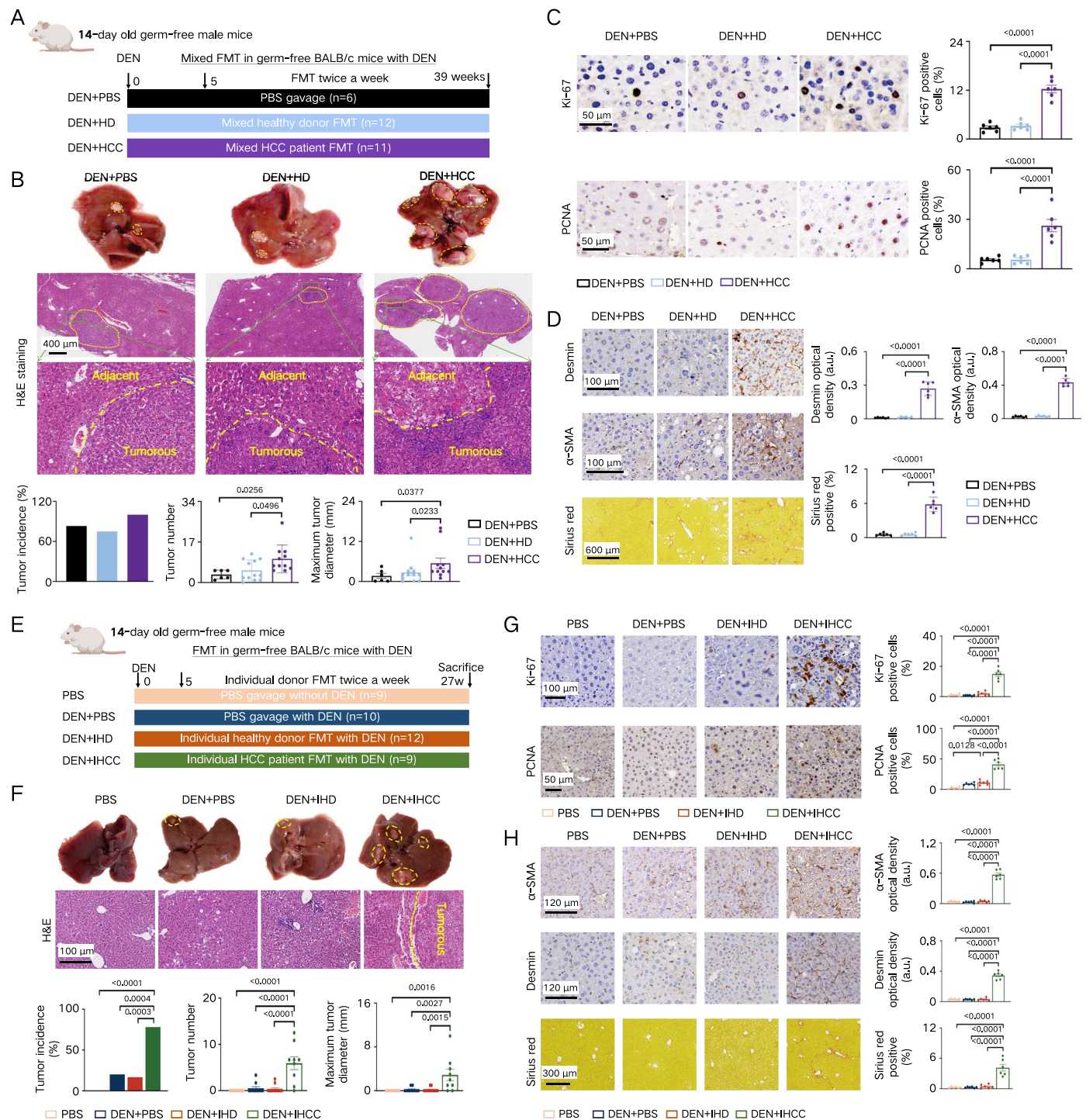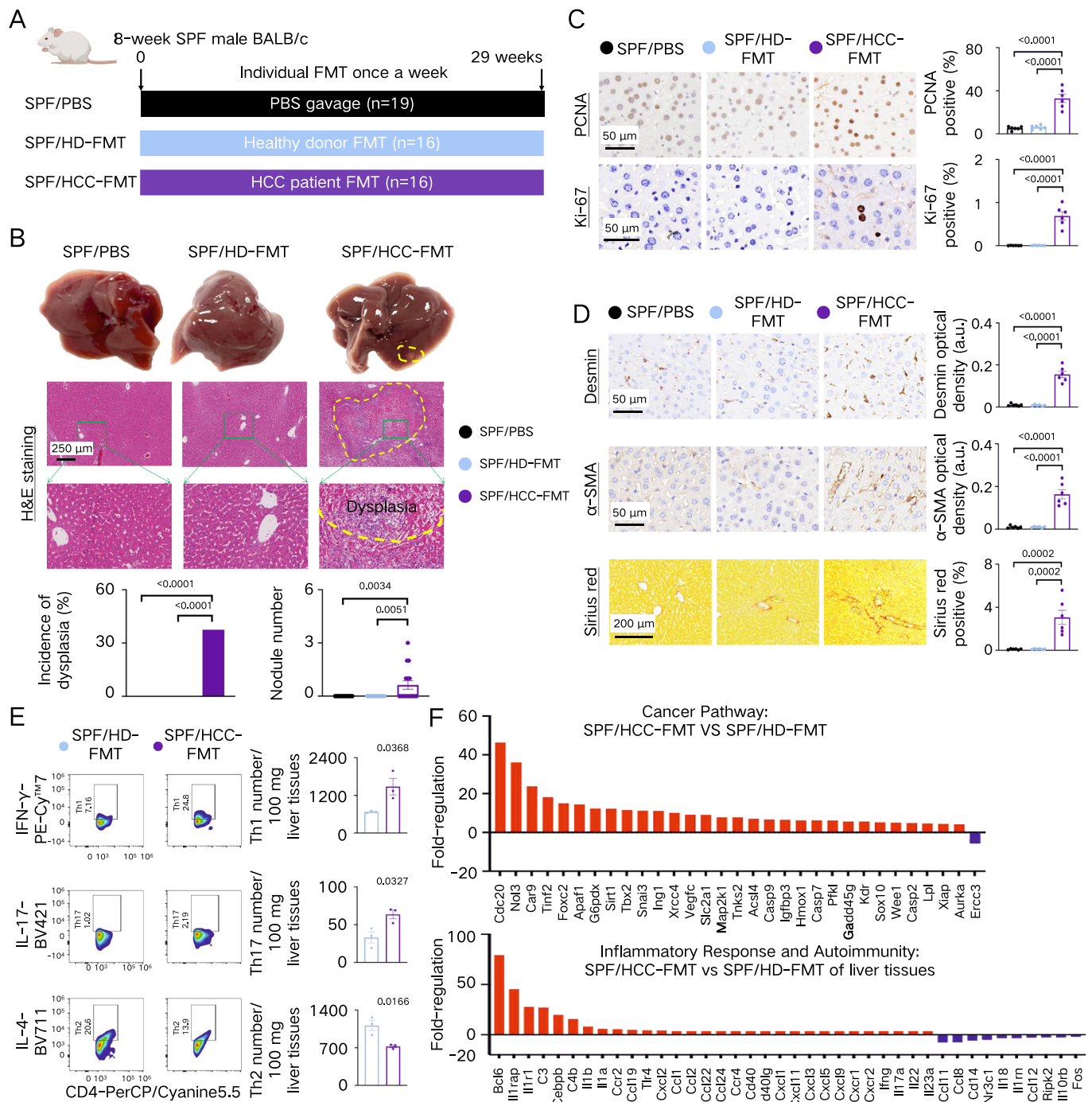
Extended Data Fig. 1 | Mixed HCC fecal microbiota transplantation and fecal microbiota from two individual HCC patients promote hepatocarcinogenesis in DEN-treated germ-free mice. (a) Design of mixed FMT experiment to DEN-treated germ-free mice (DEN+PBS group n=6; DEN+HD group n=12; DEN+HCC group n=11) and related results **(b-d)**. **(b)** Representative images of liver gross morphology (yellow circles indicate tumors) and H&E staining of mouse liver sections (yellow circles indicate tumor areas). Tumor incidence, tumor number and the maximum tumor diameter per mice. n=6 (DEN+PBS), 12 (DEN+HD), 11 (DEN+HCC). **(c)** IHC staining of Ki-67 and PCNA. n=6 biologically independent samples. **(d)** Desmin and α-SMA IHC staining, and Sirius red staining of liver sections. n=6 biologically independent samples. **(e)** Design of FMT experiment to germ-free mice with DEN treatment (PBS group n=9; DEN+PBS group n=10;

DEN+IHD group n=12; DEN+IHCC group n=9) and related results **(f-h)**. **(f)** Representative images of liver gross morphology (yellow circles indicate tumors) and H&E staining. Tumor incidence, tumor number, and maximum tumor diameter per mouse in liver. n=9 (PBS), 10 (DEN+PBS), 12 (DEN+IHD), 9 (DEN+IHCC). **(g)** Ki-67 and PCNA IHC staining. n=6 biologically independent samples. **(h)** α-SMA and Desmin IHC staining, and Sirius red staining of mouse liver sections. n=6 biologically independent samples. Data (excluding tumor incidence) are presented as mean ± SEM. Each data point in bar plots represents one mouse. Tumor incidence was calculated using Fisher's exact test. Unless otherwise stated, statistical significance was calculated using one-way ANOVA. Adjustments were made for multiple comparisons.
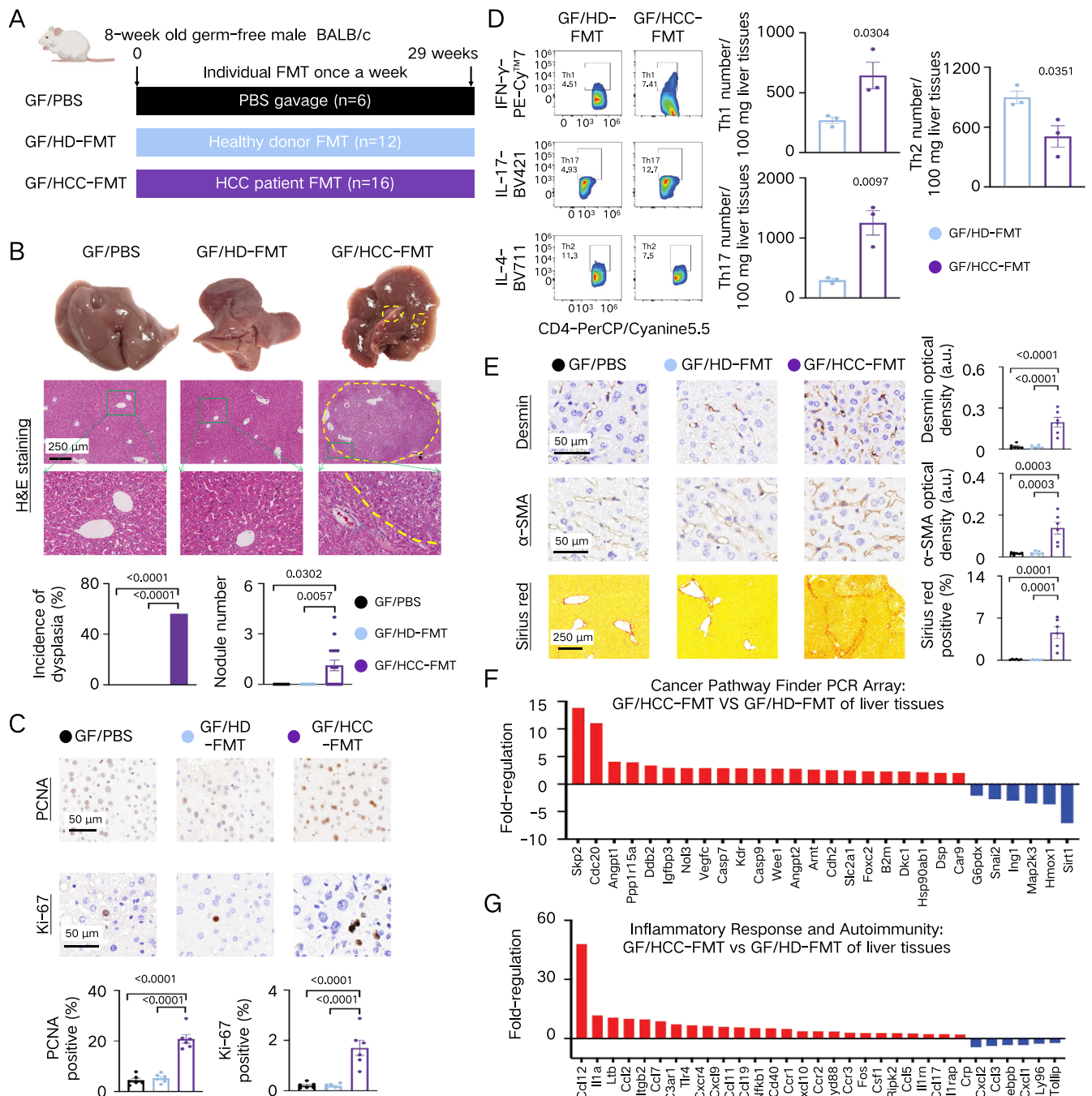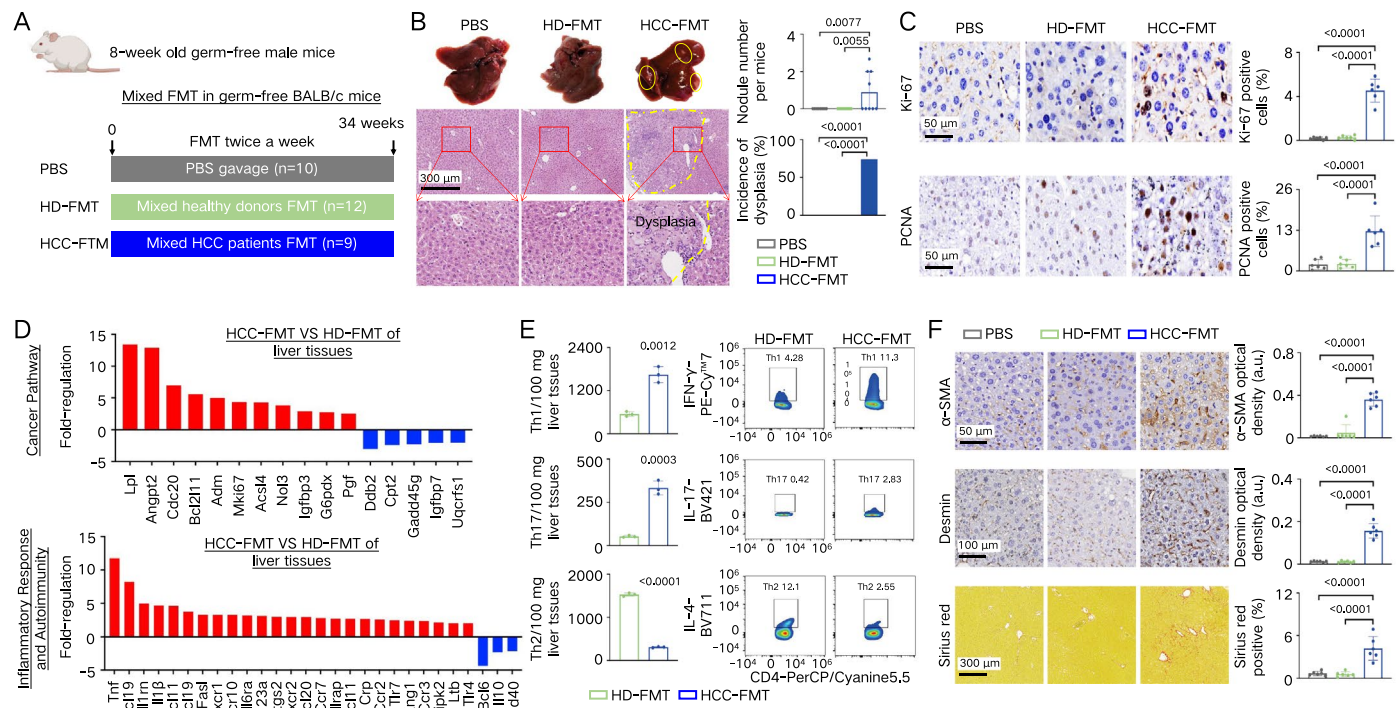
Extended Data Fig. 2 | Individual HCC patient fecal microbiota initiates liver precancerous lesions in germ-free mice without DEN treatment. (a) Design of FMT experiment to germ-free mice without DEN treatment (GF/PBS group n=6; GF/HD-FMT group n=12; GF/HCC-FMT group n=16). **(b)** Representative images of liver gross morphology (yellow circles indicate nodules), and H&E staining of mice liver sections with incidence of dysplasia and nodules number statistical results. n=6 (GF/PBS), 12 (GF/HD-FMT), 16 (GF/HCC-FMT). **(c)** IHC staining for PCNA and Ki-67. n=6 biologically independent samples. **(d)** Hepatic infiltration of Th1, Th17, and Th2 cells was evaluated by flow cytometry. n=3 biologically

independent samples. **(e)** Desmin and α-SMA IHC staining, and Sirius red staining of liver sections. n=6 biologically independent samples. **(f)** Mouse Cancer Pathway Finder Array and **(g)** Inflammatory Response and Autoimmunity PCR Array of liver tissues. **f** and **g**, n=3 independent experiments with similar results. Data (excluding incidence of dysplasia and PCR array results) are presented as mean ± SEM. Each data point in bar plots represents one mouse. Incidence of dysplasia was calculated using Fisher's exact test. Unless otherwise stated, statistical significance was calculated using one-way ANOVA. Adjustments were made for multiple comparisons.

Extended Data Fig. 3 | Individual HCC patient fecal microbiota initiates liver precancerous lesions in SPF mice without DEN treatment. (a) Design of FMT experiment to SPF mice without DEN treatment (SPF/PBS group n=19; SPF/HD-FMT group n=16; SPF/HCC-FMT group n=16). **(b)** Representative images of liver gross morphology (yellow circles indicate nodules), and H&E staining of mice liver sections. Incidence of dysplasia and number of liver nodules. n=19 (SPF/PBS), 16 (SPF/HD-FMT), 16 (SPF/HCC-FMT). **(c)** IHC staining for PCNA and Ki-67. n=6 biologically independent samples. **(d)** Desmin and α-SMA IHC staining, and Sirius red staining of liver sections. n=6 biologically independent samples.

(e) Hepatic infiltration of Th1 (n=3 biologically independent samples), Th17 (n=4 biologically independent samples), and Th2 (n=3 biologically independent samples) cells was evaluated by flow cytometry. **(f)** Mouse Cancer Pathway Finder Array and Inflammatory Response and Autoimmunity PCR Array of liver tissues. n=3 independent experiments with similar results. Data (excluding incidence of dysplasia and PCR array results) are presented as mean ± SEM. Each data point in bar plots represents one mouse. Incidence of dysplasia was calculated using Fisher's exact test. Unless otherwise stated, statistical significance was calculated using one-way ANOVA. Adjustments were made for multiple comparisons.

Extended Data Fig. 4 | Five mixed HCC fecal microbiota transplantation initiates hepatocarcinogenesis in germ-free mice without DEN treatment. (a) Design of FMT experiment to germ-free mice (PBS group n=10; HD-FMT group n=12; HCC-FMT group n=9). (b) Representative images of liver gross morphology (yellow circles indicate nodules) and H&E staining of mice liver sections. n=10 (PBS), 12 (HD-FMT), 9 (HCC-FMT). (c) IHC staining for Ki-67 and PCNA. n=6 biologically independent samples. (d) Mouse Cancer Pathway Finder PCR Array and Inflammatory Response and Autoimmunity PCR Array of liver tissues. n=3 independent experiments with similar results. (e) Th1, Th17, and Th2 cells infiltration in liver was determined by flow cytometry. n=3 biologically independent samples. (f) α-SMA and Desmin IHC staining, and Sirius red staining of liver sections. n=6 biologically independent samples. Data (excluding incidence of dysplasia and PCR array results) are presented as mean ± SEM. Each data point in bar plots represents one mouse. Incidence of dysplasia was calculated using Fisher's exact test. Unless otherwise stated, statistical significance was calculated using one-way ANOVA. Adjustments were made for multiple comparisons.
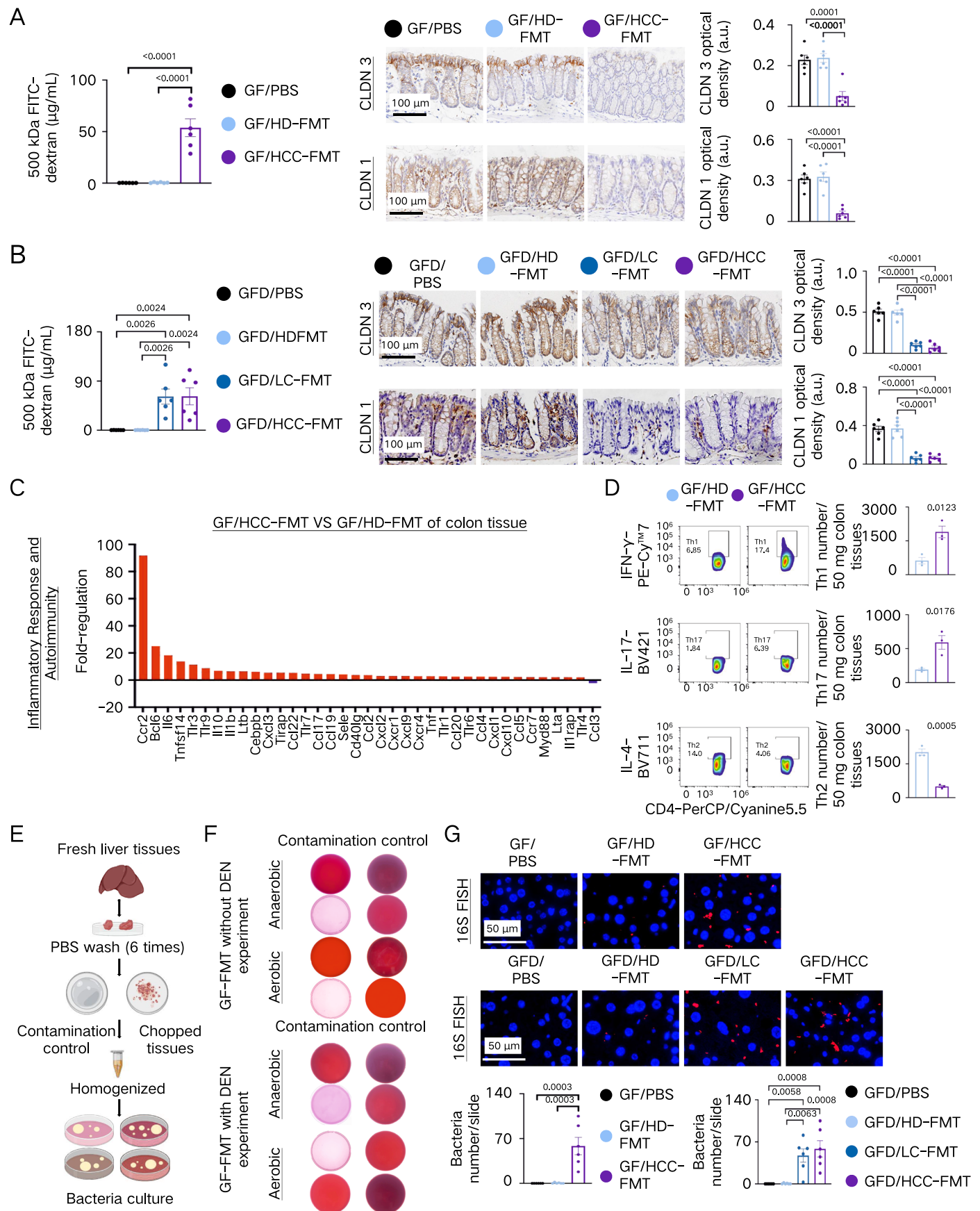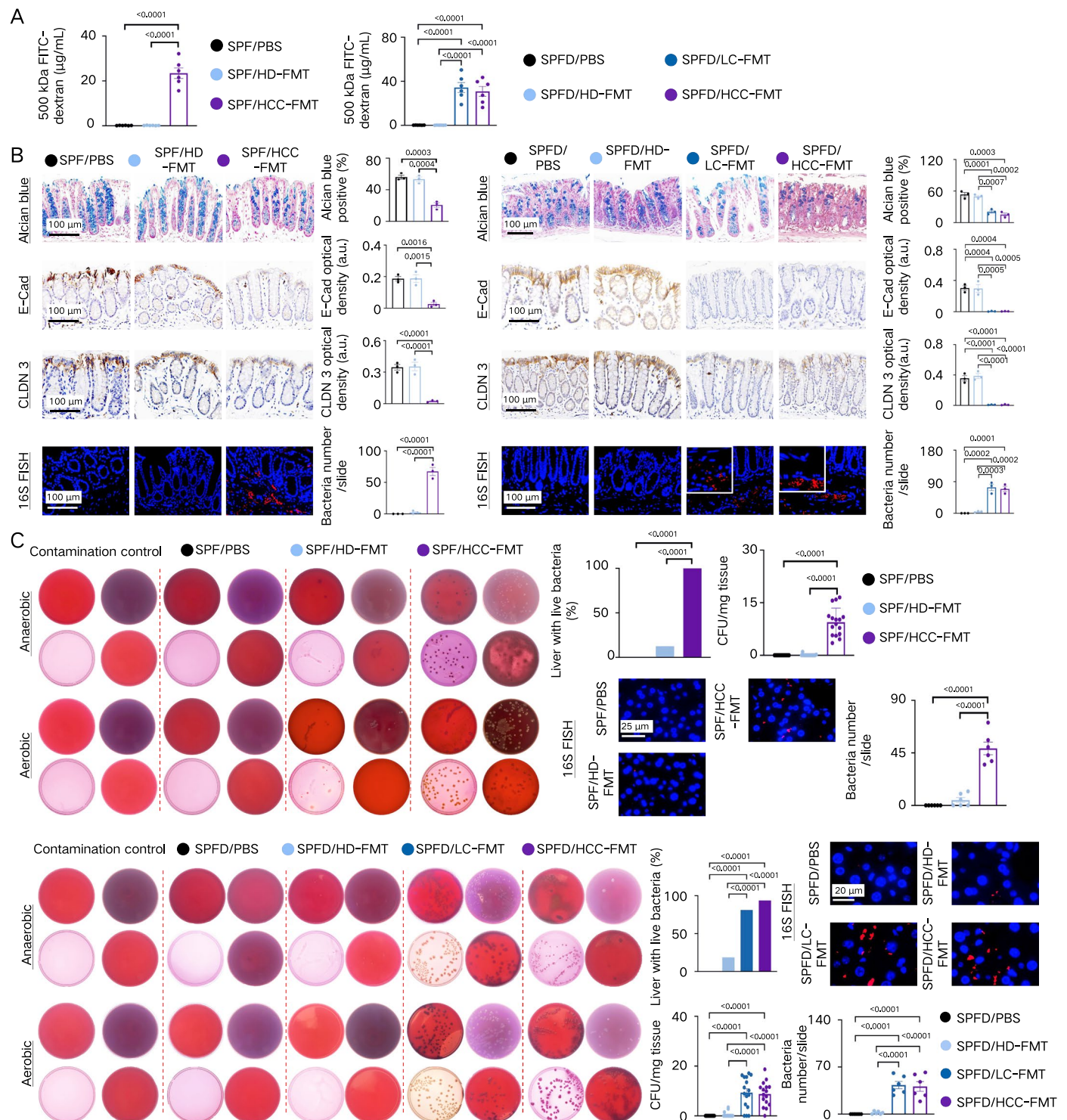
Extended Data Fig. 5 | See next page for caption.

Extended Data Fig. 5 | HCC patient fecal microbiota impairs gut barrier function, induces intestinal inflammation, and promotes bacteria translocation into liver in germ-free mice with or without DEN treatment.
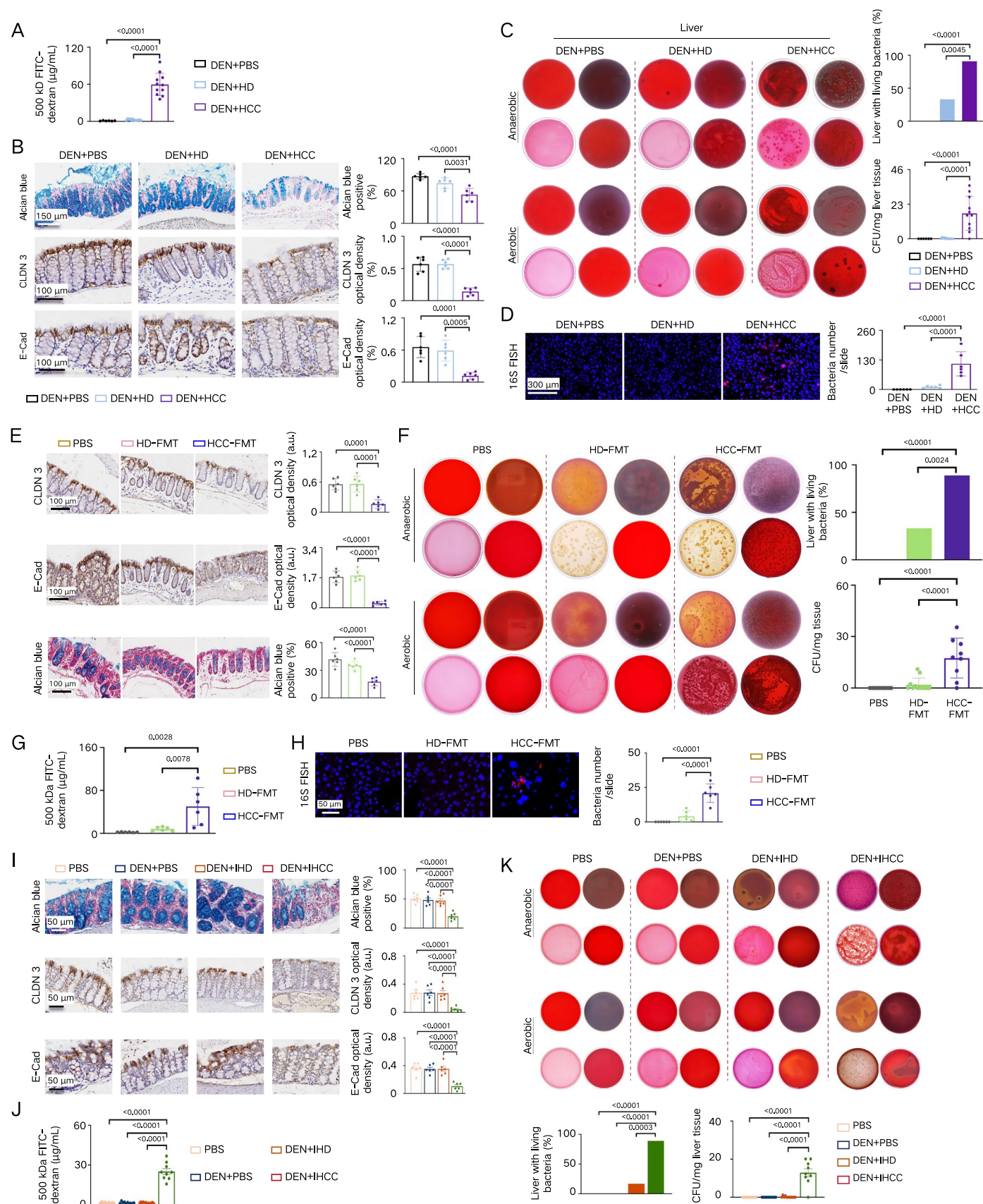(a) Gut permeability assays using 500 kDa FITC-dextran, CLDN 3 and CLDN 1 IHC staining of germ-free mice without DEN. n=6 biologically independent samples.
(b) Gut permeability assays using 500 kDa FITC-dextran, CLDN 3 and CLDN 1 IHC staining of germ-free mice with DEN. n=6 biologically independent samples.
(c) Mouse Inflammatory Response and Autoimmunity PCR Array of colon tissues. n=3 independent experiments with similar results. (d) Colon Th1, Th17,
and Th2 cells in germ-free mice without DEN was evaluated by flow cytometry. n=3 biologically independent samples. (e) Workflow of fresh liver homogenate preparation for bacteria culture. (f) PBS contamination control used in tissues bacteria culture experiment. (g) Cy3-conjugated EUB338 probe FISH detection of liver tissues. n=6 biologically independent samples. Data (excluding PCR array result) are presented as mean ± SEM. Each data point in bar plots represents one mouse. Statistical significance was calculated using one-way ANOVA. Adjustments were made for multiple comparisons.

Extended Data Fig. 6 | HCC patient fecal microbiota impairs gut barrier function and promotes bacteria translocation into liver in SPF mice with or without DEN treatment as shown in Fig. 1f and Extended Data Fig. 3a. (a) Gut permeability assay using 500 kDa FITC-dextran. n=6 biologically independent samples. **(b)** Representative pictures of Alcian blue staining, E-Cad, CLDN 3 IHC staining, and Cy3-conjugated EUB338 probe FISH of colon tissues with quantitative analysis. n=3 biologically independent samples. **(c)** Representative bacterial culture of liver tissues under anaerobic and aerobic conditions with quantitative analysis. n= 19 (SPF/PBS), 16 (SPF/HD-FMT), 16 (SPF/HCC-FMT),
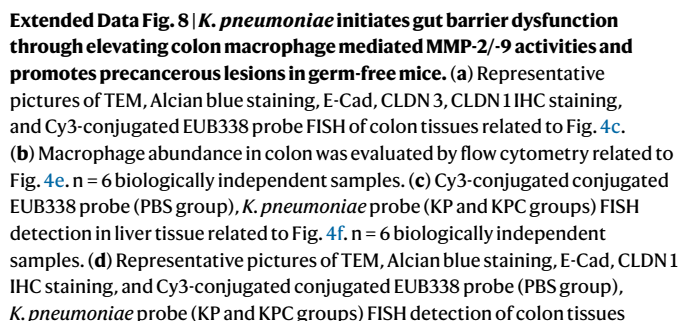
20 (SPFD/PBS), 16 (SPFD/HD-FMT), 16 (SPFD/LC-FMT), 16 (SPFD/HCC-FMT). From left to right and top to bottom, the culture plates are blood agar plate, chocolate blood agar plate, MacConkey agar plate, and Columbia blood agar plate, respectively. And, representative images of Cy3-conjugated EUB338 probe FISH detection in mice liver tissues. n=6 biologically independent samples. Data (excluding liver with live bacteria) are presented as mean ± SEM. Each data point in bar plots represents one mouse. Liver with live bacteria was calculated using Fisher's exact test. Unless otherwise stated, statistical significance was calculated using one-way ANOVA. Adjustments were made for multiple comparisons.
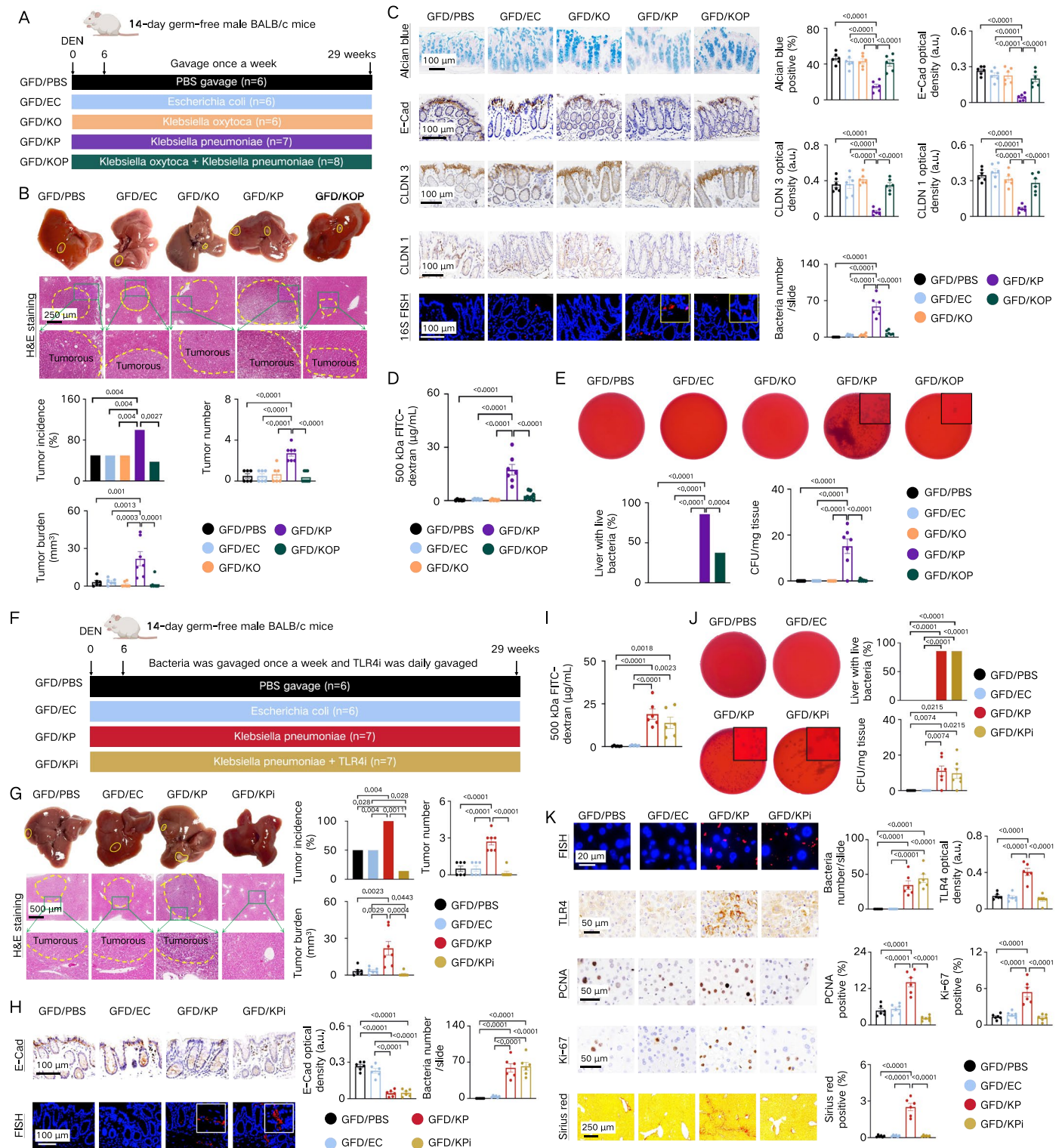
Extended Data Fig. 7 | See next page for caption.

Extended Data Fig. 7 | Mixed HCC fecal microbiota transplantation and fecal microbiota from two individual HCC patients impair gut barrier function and promotes bacteria translocation into liver in germ-free mice with or without DEN treatment. (a) Gut permeability assay using FITC-dextran. n=6 (DEN+PBS), 12 (DEN+HD), 11 (DEN+HCC). **(b)** Representative pictures of Alcian blue staining, CLDN 3 and E-Cad IHC staining of colon tissues with quantitative analysis. n=6 biologically independent samples. **(c)** Representative bacterial culture of liver tissues under anaerobic and aerobic conditions with quantitative analysis. n=6 (DEN+PBS), 12 (DEN+HD), 11 (DEN+HCC). From left to right and top to bottom, the culture plates are blood agar plate, chocolate blood agar plate, MacConkey agar plate, and Columbia blood agar plate, respectively. **(d)** Images of Cy3-conjugated EUB338 probe detection. n=6 biologically independent samples. **a–d** are related to Extended Data Fig. 1a. **(e)** Pictures of CLDN 3 and E-Cad IHC staining, and Alcian blue staining of colon tissues with quantitative analysis. n=6 biologically independent samples. **(f)** Bacterial culture of liver tissues under anaerobic and aerobic conditions with quantitative analysis. n=10 (PBS),

12 (HD-FMT), 9 (HCC-FMT). From left to right and top to bottom, the culture plates are blood agar plate, chocolate blood agar plate, MacConkey agar plate, and Columbia blood agar plate, respectively. **(g)** Gut permeability assay using FITC-dextran and **(h)** Cy3-conjugated EUB338 probe detection of liver tissue. n=6 biologically independent samples. **e-h** are related to Extended Data Fig. 4a. **(i)** Pictures of Alcian blue staining, CLDN 3 and E-Cad IHC staining of colon tissues with quantitative analysis. n=6 biologically independent samples. **(j)** Gut permeability assay using FITC-dextran. n=9 (PBS), 10 (DEN+PBS), 12 (DEN+IHD), 9 (DEN+IHCC). **(k)** Bacterial culture of liver tissues under anaerobic and aerobic conditions with quantitative analysis. n=9 (PBS), 10 (DEN+PBS), 12 (DEN+IHD), 9 (DEN+IHCC). **i-k** are related to Extended Data Fig. 1e. Data (excluding liver with live bacteria) are presented as mean ± SEM. Each data point in bar plots represents one mouse. Liver with living bacteria was calculated using Fisher's exact test. Unless otherwise stated, statistical significance was calculated using one-way ANOVA. Adjustments were made for multiple comparisons.

Extended Data Fig. 8 | *K. pneumoniae* initiates gut barrier dysfunction through elevating colon macrophage mediated MMP-2/-9 activities and promotes precancerous lesions in germ-free mice. (**a**) Representative pictures of TEM, Alcian blue staining, E-Cad, CLDN 3, CLDN 1 IHC staining, and Cy3-conjugated EUB338 probe FISH of colon tissues related to Fig. 4c. (**b**) Macrophage abundance in colon was evaluated by flow cytometry related to Fig. 4e. n = 6 biologically independent samples. (**c**) Cy3-conjugated conjugated EUB338 probe (PBS group), *K. pneumoniae* probe (KP and KPC groups) FISH detection in liver tissue related to Fig. 4f. n = 6 biologically independent samples. (**d**) Representative pictures of TEM, Alcian blue staining, E-Cad, CLDN 1 IHC staining, and Cy3-conjugated conjugated EUB338 probe (PBS group), *K. pneumoniae* probe (KP and KPC groups) FISH detection of colon tissues

with quantitative analysis related to Fig. 4h. (**e**) Representative pictures of TEM and E-Cad IHC staining of liver tissues related to Fig. 5c. Masson's trichrome staining and COL IV IHC staining of colon tissues related to Fig. 5e. (**f**) Representative pictures of PCNA and Ki-67 IHC staining related to Fig. 5g. (**g**) Representative pictures of Desmin and α-SMA IHC staining, and Sirius red staining of liver sections related to Fig. 5h. (**h**) Mouse Cancer Pathway Finder Array and Mouse Inflammatory Response and Autoimmunity PCR Array of liver tissues related to Fig. 5a. n = 3 independent experiments with similar results. Data (excluding PCR array results) are presented as mean ± SEM. Each data point in bar plots represents one mouse. Statistical significance was calculated using one-way ANOVA. Adjustments were made for multiple comparisons.

Extended Data Fig. 9 | See next page for caption.

Extended Data Fig. 9 | Antagonizing *K. pneumoniae* colonic colonization or TLR4 inhibition reverse K. pneumoniae induced-HCC development. (a) Design of *K. oxytoca* on *K. pneumoniae* induced HCC promotion in germ-free mice with DEN treatment (GFD/PBS group n=6; GFD/EC group n=6; GFD/KO group n=6; GFD/KP group n=7; GFD/KOP group n=8) and relevant results **(b−e)**. **(b)** Images of liver gross morphology (yellow circles indicate tumor area), and H&E with tumor incidence, tumor number and tumor burden. n=6 (GFD/PBS), 6 (GFD/EC), 6 (GFD/KO) 7 (GFD/KP), 8 (GFD/KOP). **(c)** Alcian blue staining, E-Cad, CLDN 3, CLDN 1 IHC, and Cy3-conjugated EUB338 probe detection with quantitative analysis. n=6 biologically independent samples. **(d)** Gut permeability assay using FITC-dextran. n=6 (GFD/PBS), 6 (GFD/EC), 6 (GFD/KO) 7 (GFD/KP), 8 (GFD/KOP). **(e)** Live bacteria culture of liver tissues on blood agar plates with quantitative analysis. n=6 (GFD/PBS), 6 (GFD/EC), 6 (GFD/KO) 7 (GFD/KP), 8 (GFD/KOP). **(f)** Design of TLR4i on *K. pneumoniae* induced HCC promotion in germ-free mice with DEN treatment (GFD/PBS group n=6; GFD/EC group n=6; GFD/KP group n=7; GFD/KPi group n=7) and relevant results **(g-k)**. **(g)** Images of liver gross morphology (yellow circles indicate tumor area), and H&E with tumor incidence, tumor number and tumor burden. n=6 (GFD/PBS), 6 (GFD/EC), 7 (GFD/KP), 7 (GFD/KPi). **(h)** E-Cad IHC and Cy3-conjugated EUB338 probe (GFD/PBS group), *E. coli* probe (GFD/EC), *K. pneumoniae* probe (GFD/KP) and GFD/KPi groups) detection of colon tissues with quantitative analysis. n=6 biologically independent samples. **(i)** Gut permeability assay using FITC-dextran. n=6 biologically independent samples. **(j)** Live bacteria culture of liver tissues on blood agar plates with quantitative analysis. n=6 (GFD/PBS), 6 (GFD/EC), 7 (GFD/KP), 7 (GFD/KPi). **(k)** Cy3-conjugated conjugated EUB338 probe (GFD/PBS group), *E. coli* probe (GFD/EC), *K. pneumoniae* probe (GFD/KP) and GFD/KPi groups) FISH, TLR4, PCNA, Ki-67 IHC, and Sirius red staining of liver sections. n=6 biologically independent samples. Data (excluding tumor incidence and liver with live bacteria) are presented as mean ± SEM. Each data point in bar plots represents one mouse. Tumor incidence and Liver with live bacteria were calculated using Fisher's exact test. Unless otherwise stated, statistical significance was calculated using one-way ANOVA. Adjustments were made for multiple comparisons.
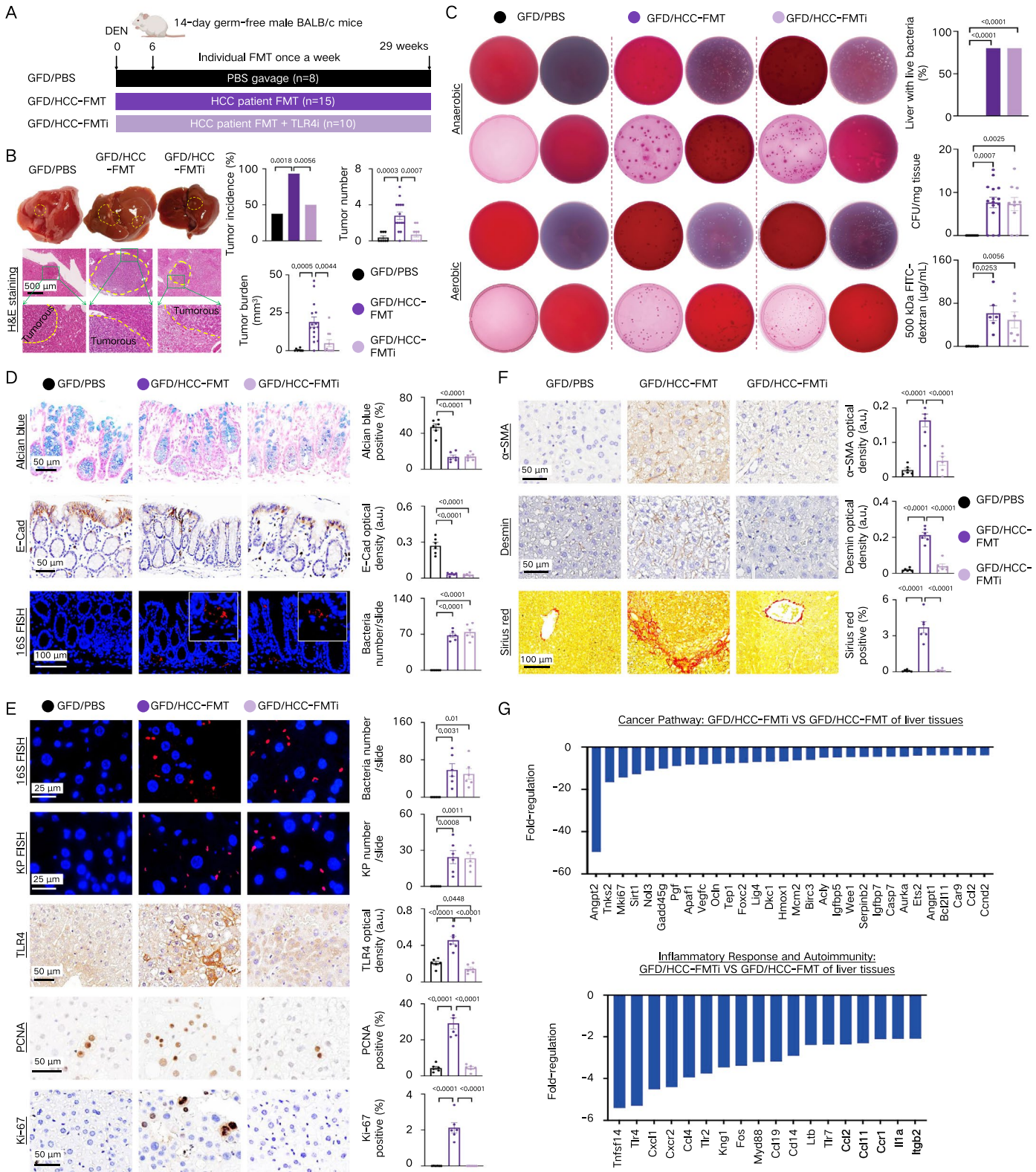
Extended Data Fig. 10 | See next page for caption.

Extended Data Fig. 10 | TLR4 inhibition reverses HCC-FMT induced-HCC development. (a) Design of TLR4i on HCC-FMT induced HCC promotion in germ-free mice with DEN treatment (GFD/PBS group n=8; GFD/HCC-FMT group n=15; GFD/HCC-FMTi group n=10) and relevant results **(b–g)**. TLR4i was daily gavaged in this experiment. **(b)** Representative images of liver gross morphology (yellow circles indicate tumor area), and H&E staining of mice liver sections with tumor incidence, tumor number, and tumor burden. n=8 (GFD/PBS), 15 (GFD/HCC-FMT), 10 (GFD/HCC-FMTi). **(c)** Representative bacterial culture of liver tissues under anaerobic and aerobic conditions with quantitative analysis. n=8 (GFD/PBS), 15 (GFD/HCC-FMT), 10 (GFD/HCC-FMTi). From left to right and top to bottom, the culture plates are blood agar plate, chocolate blood agar plate, MacConkey agar plate, and Columbia blood agar plate, respectively. Gut permeability assay using 500 kDa FITC-dextran. n=6 biologically independent samples. **(d)** Representative pictures of Alcian blue staining, E-Cad IHC staining, and Cy3-conjugated EUB338 probe FISH detection of colon tissues with quantitative analysis. n=6 biologically independent samples. **(e)** Cy3-conjugated EUB338 probe FISH, Cy3-conjugated *K. pneumoniae* probe FISH, TLR4, PCNA, Ki-67 IHC of liver sections. n=6 biologically independent samples. **(f)** α-SMA, Desmin IHC staining, and Sirius red staining of liver sections. n=6 biologically independent samples. **(g)** Mouse Cancer Pathway Finder Array and Inflammatory Response and Autoimmunity PCR Array of liver tissues. n=3 independent experiments with similar results. Data (excluding tumor incidence, liver with live bacteria and PCR array results) are presented as mean ± SEM. Each data point in bar plots represents one mouse. Tumor incidence and Liver with live bacteria were calculated using Fisher's exact test. Unless otherwise stated, statistical significance was calculated using one-way ANOVA. Adjustments were made for multiple comparisons.

nature portfolio

Corresponding author(s): JUN YU

Last updated by author(s): Sep 26, 2024

Reporting Summary

Nature Portfolio wishes to improve the reproducibility of the work that we publish. This form provides structure for consistency and transparency in reporting. For further information on Nature Portfolio policies, see our Editorial Policies and the Editorial Policy Checklist.

Statistics

For all statistical analyses, confirm that the following items are present in the figure legend, table legend, main text, or Methods section.

n/a	Confirmed	
☐	☒	The exact sample size (*n*) for each experimental group/condition, given as a discrete number and unit of measurement
☐	☒	A statement on whether measurements were taken from distinct samples or whether the same sample was measured repeatedly
☐	☒	The statistical test(s) used AND whether they are one- or two-sided *Only common tests should be described solely by name; describe more complex techniques in the Methods section.*
☒	☐	A description of all covariates tested
☒	☐	A description of any assumptions or corrections, such as tests of normality and adjustment for multiple comparisons
☐	☒	A full description of the statistical parameters including central tendency (e.g. means) or other basic estimates (e.g. regression coefficient) AND variation (e.g. standard deviation) or associated estimates of uncertainty (e.g. confidence intervals)
☐	☒	For null hypothesis testing, the test statistic (e.g. *F*, *t*, *r*) with confidence intervals, effect sizes, degrees of freedom and *P* value noted *Give P values as exact values whenever suitable.*
☒	☐	For Bayesian analysis, information on the choice of priors and Markov chain Monte Carlo settings
☒	☐	For hierarchical and complex designs, identification of the appropriate level for tests and full reporting of outcomes
☒	☐	Estimates of effect sizes (e.g. Cohen's *d*, Pearson's *r*), indicating how they were calculated

Our web collection on statistics for biologists contains articles on many of the points above.

Software and code

Policy information about availability of computer code

Data collection	Living image v4.3.1 (Perkin Elmer), Attune™ NxT Software v3.1.1 (ThermoFisher Scientific), Image Lab software v6.1.0 (Bio-rad), QuantStudio Real Time PCR software v1.7.2 (Applied Biosystems), EMIP-SP (Hitachi), cellSens™ FV imaging software v3.1.1 (Olympus)
Data analysis	FlowJo v10.9.0, ImageJ v1.51, GraphPad Prism, v10.3.1, Pymol v2.1, Biacore T200 Evaluation Software v2.0

For manuscripts utilizing custom algorithms or software that are central to the research but not yet described in published literature, software must be made available to editors and reviewers. We strongly encourage code deposition in a community repository (e.g. GitHub). See the Nature Portfolio guidelines for submitting code & software for further information.

Data

Policy information about availability of data

All manuscripts must include a data availability statement. This statement should provide the following information, where applicable:
- Accession codes, unique identifiers, or web links for publicly available datasets
- A description of any restrictions on data availability
- For clinical datasets or third party data, please ensure that the statement adheres to our policy

The datasets generated during and/or analysed during the current study are available from the corresponding authors upon request. All related raw data has been deposited to the public datasets with accession number.

Research involving human participants, their data, or biological material

Policy information about studies with <u>human participants or human data</u>. See also policy information about <u>sex, gender (identity/presentation), and sexual orientation</u> and <u>race, ethnicity and racism</u>.

Reporting on sex and gender	Yes
Reporting on race, ethnicity, or other socially relevant groupings	No
Population characteristics	Age matched. And, there are no restrictions on gender. For detailed information, please refer to Supplementary Table S1-S4.
Recruitment	The exclusion criteria were as follows: 1) use of antibiotics within the past 3 months; 2) had received prior cancer treatment; 3) had a history of other cancers; 4) presence of intrahepatic cholangiocarcinoma and had a history of gastrointestinal operations. No self-selection bias was exist.
Ethics oversight	Written informed consent was obtained for all human samples and this study was approved by the Ethics Committee of the First Affiliated Hospital of Sun Yat-sen University (ID Number: [2024]141 and [1992]151). Corresponding compensation was provided to participants.

Note that full information on the approval of the study protocol must also be provided in the manuscript.

Field-specific reporting

Please select the one below that is the best fit for your research. If you are not sure, read the appropriate sections before making your selection.

☒ Life sciences   ☐ Behavioural & social sciences   ☐ Ecological, evolutionary & environmental sciences

For a reference copy of the document with all sections, see <u>nature.com/documents/nr-reporting-summary-flat.pdf</u>

Life sciences study design

All studies must disclose on these points even when the disclosure is negative.

Sample size	No statistical methods were used to pre-determine sample sizes but our sample sizes are similar to those reported in previous publication.
Data exclusions	No data points were excluded.
Replication	All in vitro experiments were repeated three times as three independent experiments unless otherwise stated. For in vitro experiments, all attempts at replication were successful .For in vivo experiments, all experiments were successful without replication.
Randomization	Mice used in the experiments were litter mates and age-matched, and randomized into control and experimental groups. All samples were allocated in random.
Blinding	Blinding was not possible in experiments since the same investigator performed the experiment and data analysis.

Reporting for specific materials, systems and methods

We require information from authors about some types of materials, experimental systems and methods used in many studies. Here, indicate whether each material, system or method listed is relevant to your study. If you are not sure if a list item applies to your research, read the appropriate section before selecting a response.

Materials & experimental systems

n/a	Involved in the study
☐	☒ Antibodies
☐	☒ Eukaryotic cell lines
☒	☐ Palaeontology and archaeology
☐	☒ Animals and other organisms
☒	☐ Clinical data
☒	☐ Dual use research of concern
☒	☐ Plants

Methods

n/a	Involved in the study
☒	☐ ChIP-seq
☐	☒ Flow cytometry
☒	☐ MRI-based neuroimaging

Antibodies

Antibodies used	Secondary antibodies (1:5000) (HRP-linked anti-mouse IgG #7076, HRP-linked anti-rabbit IgG #7074, Cell Signaling Technology, USA) were used. TLR4 (HY-P80918, MCE), MyD88 (4283, Cell Signaling Technology), NF-κB P65 (ab32536, Abcam), NF-κB p-P65 (ab76302, Abcam), β-actin (4970, Cell Signaling Technology), GST (2624, Cell Signaling Technology), PCNA (ab29, Abcam), COL IV (ab6586, Abcam), ZO-1 (13663, Cell Signaling Technology), E-Cad (14472, Cell Signaling Technology), Fibronectin (ab268020, Abcam). Detail information of antibodies used in the study was shown in Supplementary Table S5.
Validation	All antibodies were obtained from commercial sources, and vendors have shown validation on their websites.

Eukaryotic cell lines

Policy information about cell lines and Sex and Gender in Research

Cell line source(s)	Human HCC cell lines Hep 3B (#HB-8064, American Type Culture Collection, USA), Huh 7 (#01042712, Sigma-Aldrich, USA), normal colonic epithelial cells NCM460 (#NCM460D, Incell, USA), and THP-1 monocyte cells (#TIB-202, American Type Culture Collection, USA).
Authentication	All cell lines used were authenticated by ATCC and Incell (STR profiling).
Mycoplasma contamination	All cell lines tested negative for mycoplasma contamination.
Commonly misidentified lines (See ICLAC register)	No commonly misidentified cell lines were used in this study.

Animals and other research organisms

Policy information about studies involving animals; ARRIVE guidelines recommended for reporting animal research, and Sex and Gender in Research

Laboratory animals	For germ-free mice without DEN treatment, 8-week old male germ-free BALB/c mice were selected for FMT or bacteria gavage. For SPF mice without DEN treatment, 8-week old male SPF BALB/c or C57BL/6J mice were selected for FMT or bacteria gavage. For germ-free mice with DEN treatment, 14-day old male germ-free BALB/c mice were selected. For SPF mice with DEN treatment, 14-day old male SPF BALB/c or C57BL/6J mice were selected. Mice were raised in SPF or sterile facilities, following a cycle of 12 hours light and 12 hours dark. Food (for SPF mice: #1010058, Jiangsu Xietong, China; for germ-free mice: 1019018#, Jiangsu Xietong, China) and sterile water were provided ad libitum.
Wild animals	This study did not involve wild animals.
Reporting on sex	Only male mice were used in the study.
Field-collected samples	No field collected samples were used in the study.
Ethics oversight	All experiments were approved by the Animal Experimentation Ethics Committee of The First Affiliated Hospital of Sun Yat-sen University (ID Number: [2023]361 and [2024]141) or Shenzhen Jingtuo Biotechnology Co., Ltd (ID Number: [2023]51), which required maximum tumor volume not exceeding 2,000 mm3, maximum diameter not exceeding 15 mm, and tumor weight not exceeding 5% of body weight.

Note that full information on the approval of the study protocol must also be provided in the manuscript.

Flow Cytometry

Plots

Confirm that:

☒ The axis labels state the marker and fluorochrome used (e.g. CD4-FITC).

☒ The axis scales are clearly visible. Include numbers along axes only for bottom left plot of group (a 'group' is an analysis of identical markers).

☒ All plots are contour plots with outliers or pseudocolor plots.

☒ A numerical value for number of cells or percentage (with statistics) is provided.

Methodology

Sample preparation	Multicolor flow cytometry was performed to study the immune cell types in liver and colon tissues. Single-cell suspension from liver and colon tissues were prepared with Liver Dissociation Kit (#130-105-807, Miltenyi Biotec, Germany) or Lamina Propria Dissociation Kit (#130-097-410, Miltenyi Biotec, Germany), respectively. THP-1 monocyte cells were cultured in RPMI 1640 medium. THP-1 cells are differentiated into macrophages by 3 days incubation with 150 nM phorbol ester, following by morphological observation and flow cytometry to evaluate CD14 expression.

Instrument	Attune NxT Acoustic Focusing Cytometer (ThermoFisher Scientific, USA).
Software	FlowJo v10.9.0 software (FlowJo, LLC, USA).
Cell population abundance	CD45 positive cells from each mice liver or colon (100,000-200,000 cells) were used to further identify different kinds of immune cells by its markers.
Gating strategy	Gating strategy of Th cells from mice live tissue and colonic tissue, including Th1 cellls (FVS510- CD45+ CD4+ IFN-γ+), Th2 cells (FVS510- CD45+ CD4+ IL-4+), Th17 cells (FVS510- CD45+ CD4+ IL-17+). Gating strategy of THP-1 induced macrophages in vitro, macrophage cells (FVS510- CD14+). Gating strategy of macrophages from mice colonic tissue, macrophage cells (FVS510- CD45+ MHC II+ CD11b+ Ly-6C-).

☒ Tick this box to confirm that a figure exemplifying the gating strategy is provided in the Supplementary Information.